Remote Sensing of Environment 298 (2023) 113824

Contents lists available at ScienceDirect

Remote Sensing of Environment

journal homepage: www.elsevier.com/locate/rse

Modeling forest canopy surface retrievals using very high-resolution spaceborne stereogrammetry: (II) optimizing acquisition configurations

Tiangang Yin[a,b,c,d,*], Paul M. Montesano[b,e], Bruce D. Cook[b], Eric Chavanon[f], Christopher S. R. Neigh[b], David Shean[g], Dongju Peng[h], Nicolas Lauret[f], Ameni Mkaouar[b,i], Omar Regaieg[f], Zhijun Zhen[f], Rongjun Qin[j], Jean-Philippe Gastellu-Etchegorry[f], Douglas C. Morton[b]

[a] Earth System Science Interdisciplinary Center, University of Maryland, College Park, MD 20740-3823, USA
[b] Biospheric Science Laboratory, NASA Goddard Space Flight Center, Greenbelt, MD, USA
[c] Department of Land Surveying and Geo-Informatics, The Hong Kong Polytechnic University, Hung Hom, Hong Kong
[d] JC STEM Lab of Earth Observations, Department of Land Surveying and Geo-Informatics, The Hong Kong Polytechnic University, Hung Hom, Hong Kong
[e] Science Systems and Applications, Inc., Lanham, MD, USA
[f] Centre d'Etudes Spatiales de la Biosphère – UT3, CNES, CNRS, IRD, Université de Toulouse, 31401 Toulouse Cedex 9, France
[g] Department of Civil and Environmental Engineering, University of Washington, Seattle, WA, USA
[h] Earth Observatory of Singapore, Nanyang Technological University, Singapore
[i] Goddard Earth Sciences and Technology Research II, University of Maryland Baltimore County, Baltimore, MD 21250, USA
[j] Department of Civil, Environmental and Geodetic Engineering, The Ohio State University, Columbus, OH, USA

ARTICLE INFO

Edited by Jing M. Chen

Keywords:
Radiative transfer model
Photogrammetry
Stereogrammetry
Surface elevation
Canopy structure
Open forest
Closed forest
Worldview
LiDAR
NASA STV
Solar zenith angle
Convergence angle
New mission
Camera model
Jitter
Resolution

ABSTRACT

The optimal configurations for very high-resolution (VHR, <2 m) spaceborne imagery collection to support stereogrammetry over complex forested terrain remain uncertain. We conducted a comprehensive sensitivity study of digital surface models (DSMs) derived from thousands of simulated along-track VHR stereopairs over two lidar-reconstructed forested scenes of closed and open canopies using the discrete anisotropic radiative transfer (DART) model. We evaluated the influence of convergence angle (CA), solar illumination, and image resolution on the derived DSM accuracy relative to the reference DSM and digital terrain model (DTM) products from airborne lidar data. Our results confirmed that the CA is the most critical acquisition parameter for DSM accuracy. Compared to the frequently used CA of $\sim 35^{\circ}$ for along-track stereopair acquisitions by WorldView satellites, a smaller CA can provide better accuracy for forest canopy shape estimation by reducing occlusions and mitigating radiometric variance caused by the bidirectional reflectance characteristics of vegetation. For forested scenes over relatively flat terrain, oblique solar zenith angles ($50-70^{\circ}$) yielded more consistent DSMs with better accuracy, whereas images with a hotspot configuration generated elevations that were closer to the DTM. Image pairs with smaller ground sample distance (GSD) improved the DSM accuracy, and combinations of small (nadir) and large (off-nadir) GSDs had accuracy between those derived from homogeneous GSDs. These simulation results suggest that available global archives of DSMs from VHR stereo imagery collected under a range of acquisition configurations will yield inconsistent estimates of canopy surfaces. This study also provides a benchmark dataset and configuration guide for 1) selecting existing data to retrieve the forest canopy surface shape, and 2) defining requirements for future satellite missions to characterize the forest canopy surface using stereogrammetry.

1. Introduction

Satellite remote sensing provides an efficient way to retrieve global three-dimensional (3-D) vegetation canopy structure (Hall et al., 2011) needed to understand carbon storage in aboveground biomass and variability in vegetation function (Gamon et al., 1995; Paruelo et al., 2004; Purves and Pacala, 2008). Active sensing platforms provide measures of vegetation structure and density, including: the P-band synthetic aperture radar (SAR) onboard the BIOMASS mission (Le Toan et al., 2011; Quegan et al., 2019); the lidar waveforms acquired from the

---

[*] Corresponding author at: Earth System Science Interdisciplinary Center, University of Maryland, College Park, MD 20740-3823, USA.
E-mail address: tiangang.yin@polyu.edu.hk (T. Yin).

https://doi.org/10.1016/j.rse.2023.113824
Received 2 June 2022; Received in revised form 3 September 2023; Accepted 17 September 2023

Geoscience Laser Altimeter System (GLAS) carried on the Ice, Cloud and land Elevation Satellite (ICESat) (Harding and Carabajal, 2005; Schutz et al., 2005; Simard et al., 2011; Zwally et al., 2002) and from the Global Ecosystem Dynamics Investigation (GEDI) (Dubayah et al., 2020; Liu et al., 2021); and the detected photons acquired from the Advanced Topographic Laser Altimeter System (ATLAS) instrument on ICESat-2 (Abdalati et al., 2010; Malambo and Popescu, 2021; Neuenschwander and Pitts, 2019; Neumann et al., 2019). Although lidar data have been widely used to study aboveground biomass and leaf area index (LAI) (Yan et al., 2019), spaceborne sensors have limited spatial coverage and resolution because of the relatively large footprint sizes (approximately 25–100 m in diameter) and large gaps between each beam track (Markus et al., 2017; Qi and Dubayah, 2016). SAR tomography provides more complete coverage but at moderate resolution; the BIOMASS mission will provide aggregated products at 200 m resolution (Quegan et al., 2019). Fine-scale spatial detail on the horizontal surface and vertical structure of vegetation, therefore, remains a challenge for current and planned remote sensing instruments. Techniques such as stereogrammetry could provide a high-resolution digital surface model (DSM) to complement information on the vertical structures of vegetation acquired from active sensors, such as 1) estimating canopy height by subtracting an existing lidar-derived digital terrain model (DTM) from the stereo-derived DSM, and 2) reducing uncertainties in estimates of LAI (Jiang et al., 2021) and aboveground biomass (Bruening et al., 2021).

In recent years, very high-resolution (VHR) platforms with a spatial resolution of <2 m have attracted considerable interest in stereogrammetry methods to deliver continental to global-scale DSMs and quantify fine-scale changes in vegetation and ice surfaces (NASA, 2021; Neigh et al., 2014, 2016; Persson and Perko, 2016; Shean et al., 2016; St-Onge et al., 2008; Winsemius et al., 2019). For example, the ArcticDEM (Morin et al., 2016; Porter et al., 2018) and Reference Elevation Model of Antarctica (REMA, Howat et al., 2019) generated from Maxar VHR imagery (WorldView and GeoEye), provide DSM mosaics and strips with <10 m resolution and <1 m accuracy as a benchmark for detecting changes in the polar regions. In addition, elevations derived from VHR images were used to monitor glacier mass changes and ocean-induced basal melting (Berthier et al., 2023; Bolch et al., 2011; Hugonnet et al., 2021; Shean et al., 2019, 2020) and ocean-induced ice shelf basal melting (Shean et al., 2019). A summary of VHR satellite platforms is provided in Appendix A. Within the next decade, planned satellite constellations will increase the capacity for VHR stereo (Garzaniti et al., 2021). For example, the stereoscopic constellation of ZY-3 and GF-7 can greatly improve the observation frequency and data acquisition efficiency (Li et al., 2021; Zhao et al., 2022); The Planet SkySat-C constellation includes 19 push-frame VHR imagers with 0.7 m GSD that can collect along-track triplet stereo and same-day multi-view, multi-sensor collections (Bhushan et al., 2021); WorldView-Legion (Maxar) includes six satellites to collect 30 cm resolution imagery, providing up to 15 revisits per day (Duro et al., 2021); Similarly, Pléiades Neo (Airbus) includes four identical platforms with 30 cm resolution panchromatic and 1.2 m multispectral (6 bands) satellite imagery (Jérôme, 2019); a follow-on mission CO3D will consist four small satellites and collect multispectral data at resolutions of 50 cm (visible) and 1 m (near-infrared) (Lebègue et al., 2020). Improvements in spatial resolution and global data coverage may yield important advances in the availability of DSMs from VHR stereogrammetry. However, other factors also influence the accuracy of derived surface heights.

The accuracy of the surface elevations derived from VHR stereogrammetry depends on both reconstruction algorithms and acquisition configurations (Lazaros et al., 2008; Qin, 2019). The algorithms and their parameter settings are usually predefined for global-scale DSM production, such as the algorithm configurations of the NASA Ames Stereo Pipeline (ASP, Beyer et al., 2018; Moratto et al., 2010; Shean et al., 2016) that are implemented on the NASA Center for Climate Simulation's Advanced Data Analytics Platform (ADAPT) (Montesano et al., 2017, 2019). The acquisition configurations vary for each satellite instrument (e.g., resolution, field of view, time of acquisition, and convergence angle), and the optimal configurations differ based on landscape complexity (e.g., topography and landcover characteristics).

Several past efforts have studied the influence of stereo image acquisition characteristics on the accuracy of VHR-derived DSMs in urban settings, due in part to greater stereopair data availability over urban areas, such as the multi-view benchmark dataset from Johns Hopkins University Applied Physics Lab (Bosch et al., 2016). These studies have considered multiple factors, including spatial resolution, base-to-height (B/H) ratio, convergence angle (CA), and solar incident angle (Qin, 2019; Toutin, 2004). However, the optimal configuration for stereo image acquisition in urban settings may not be suitable for forested landscapes. Compared to urban environments, forests have different horizontal and vertical complexity with different directional reflectance properties. The optimal configurations for forests could also differ depending on latitude and forest type, given the distinct differences in forest composition, crown shape, fractional cover, and background reflectance.

Previous studies on stereo surface retrievals over vegetation have explored limited configurations in specific case studies. For example, the along-track VHR stereo reconstruction of GeoEye and WorldView (~0.5 m resolution) over Australian tropical savannas severely underestimated tree presence and canopy height (Goldbergs et al., 2019). The best accuracy of VHR stereo of the boreal open canopy was observed with oblique solar zenith angle (SZA) ranging from 55° to 65° (Montesano et al., 2017). A slight forward-backward CA of 12° from the tri-stereo configuration of Pléiades (Perko et al., 2014) was found to be favorable in terms of accuracy and completeness over the Ticino site in Switzerland, whereas a larger ~25° convergence angle over the Ljubljana site in Slovenia created large gaps with missing data (Piermattei et al., 2018). To date, the optimal configurations to support stereogrammetry over complex forested landscapes have not been fully explored because of three primary challenges:

1) the structural and radiometric complexity of vegetation features, including the effect of anisotropic reflectance (Roujean et al., 1992; Schaepman-Strub et al., 2006; Wu et al., 2019).
2) the limited sensor and acquisition configurations of existing VHR stereo data, such as the most frequently used ~ 35° CA of WorldView.
3) the lack of contemporaneous high-fidelity reference surface elevation data to evaluate the VHR stereo results.

These challenges must be addressed to collect datasets for a comprehensive study of the factors associated with optimal vegetation surface structure retrieval, and for designing future VHR stereo satellite missions.

Physical-based radiative transfer models (RTM) can accurately simulate high-resolution remote sensing measurements over forests across the full range of configurations. In a previous study, Yin et al. (2023) enhanced the discrete anisotropic radiative transfer (DART) model (Gastellu-Etchegorry et al., 1996, 2015, 2017) to simulate VHR stereopairs by implementing sensor models described by rational polynomial coefficients (RPCs) (Fraser and Hanley, 2003). In that work, DSMs derived from simulations were comparable to those derived from WorldView stereopairs for two forested sites, confirming DART's capability to simulate realistic VHR imagery over various forest types.

Here, we conduct a comprehensive sensitivity analysis to identify optimal configurations for along-track VHR stereopair acquisitions to capture closed- and open-canopy forest surface structures. We begin with an analysis of the geometric configuration of image acquisition, including solar zenith angle (SZA), sun-view2 angle (SV2A), and CA based on stereopair combinations from thousands of simulated images with a 0.5 m ground sample distance (GSD). Subsequently, we considered the influence of spatial resolution (0.5, 1.0, and 2.0 m), and geolocation offsets typical of RPC replacement from pushbroom jitter or associated with data acquisitions from different orbits (averaged 0.5 and 5 m, respectively) on the derived DSM from simulated stereopairs. These simulation data and results provide a relatively complete understanding of the tradeoffs in stereo image acquisition over forests and serve as a benchmark for conducting further studies, including an in-depth understanding of VHR stereo capacity, fusion with other sensors and platforms, and advanced algorithm development (e.g., deep learning) for vegetation surface structure retrieval.

2. Study methods and configurations

2.1. Study sites and background

We simulated stereopair images over two 16-ha study sites representing closed- and open-canopy temperate forests (Fig. 1). The closed canopy forest is located at the Smithsonian Environmental Research Center (SERC, Edgewater, MD, USA, Lat: 38.890, Lon: −76.561, a subset of the 36-ha scene used in Yin et al., 2023), and the open canopy is located at the Gus Pearson Natural Area (GPNA, Flagstaff, AZ, USA, Lat: 35.273, Lon: −111.745). SERC is a closed-canopy, mixed-species deciduous forest, whereas GPNA is an open-canopy forest of evergreen *Pinus ponderosa* with approximately 50% fractional canopy cover. Each forested scene was reconstructed in DART using 0.5 m voxels, and the leaf area density (LAD) in each voxel was estimated using multi-path lidar data from Goddard's Lidar, Hyperspectral, and Thermal (G-LiHT) Airborne Imager (Cook et al., 2013) and the PVlad model (Yin et al., 2022).

Here, we compared DSMs generated from stereopair simulations over the SERC and GPNA forest sites to the reference DSM and DTM derived from the G-LiHT lidar data at 1.0 m resolution. In addition, as shown in Appendix B, we ran simulations using a bare-earth scene by removing all aboveground vegetation over GPNA, and compared it with the reference DTM. This terrain-only simulation removed the influence of the complex structure and bidirectional reflectance property of vegetation as a reference case to investigate the impact of forest vegetation on stereo reconstruction. Note that both SERC and GPNA have relatively flat terrain, with mean slopes of $< 5^\circ$ across each study area. The sensor and environmental configurations of DART simulations, RPC simulation methods, DSM generation methods and result evaluation metrics ($Bias_z$, RMSE' against reference DSM_{ref} and DSM_{ref} derived from G-LiHT data) have been elaborated in Yin et al. (2023). DSM_{gen} represents the stereo-generated DSM of 1.0 m GSD, and DSM_{cr} is derived after the co-registration of DSM_{gen} to the reference DSM_{ref} or DTM_{ref}. Previous comparisons demonstrated consistent DSM_{gen} between the three

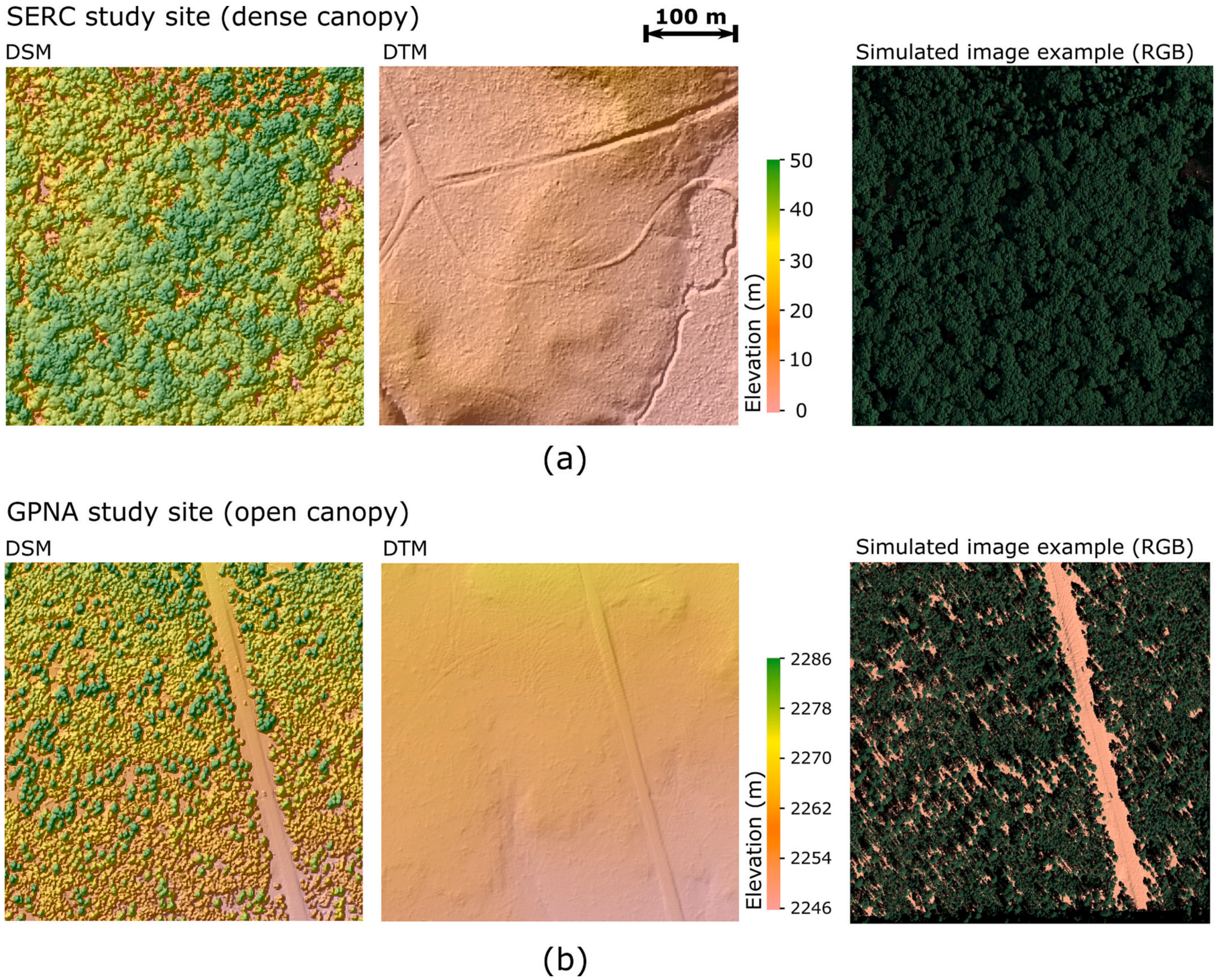

Fig. 1. DSM (left), DTM (center) and DART-simulated image (right, the true colour RGB bands of WorldView) for the study sites (a) Smithsonian Environmental Research Center (SERC), and (b) Gus Pearson Natural Area (GPNA).

simulated and WorldView along-track stereopairs, with <1.6 m in vertical bias, <1.0 m in *RMSE*’ RMSE’ and <0.07 in correlation coefficient. These results built a basis for the current study using the same $Bias_z$ and $RMSE'$ as the evaluation metrics.

2.2. Sensitivity study of configurations

This sensitivity study seeks to identify the optimal along-track pushbroom VHR satellite stereopair (restricted to two cameras) collection configuration for forest canopy shape retrieval at 1 m GSD. For all DART simulations, we adopted a broadband panchromatic spectral domain (450–800 nm) with a leaf reflectivity of 0.263 and a soil reflectivity of 0.097. In addition, we defined a clear-sky atmosphere using the USSTD76 gas and RURAL aerosol (visibility of 23 km) model (Berk et al., 1987; Gastellu-Etchegorry et al., 2017; Grau and Gastellu-Etchegorry, 2013).

2.2.1. Sensitivity study of geometric configurations

In this study, the platform trajectory was assumed to be along the north-south direction (view azimuth angle of 0° or 180°). One of the two cameras (Yin et al., 2015) has a nadir orientation (view1), whereas the other camera (view2) has an oblique view zenith angle (VZA) from 5° to 35° with a step of 5°. To test small CA geometry, we also prepared additional view2 VZA from 1° to 10° with a step of 1° for GPNA. This configuration extends in both the north and south directions to account for the ascending and descending orbits. For the solar direction over each site, we simulated daytime steps ranging from 8 AM to 2 PM with an interval of 1 h (daylight saving GTM-5 for SERC and GTM-7 for GPNA) for the 20th day of each month from the summer solstice (June) to the winter solstice (December), in the year of the reference G-LiHT acquisitions (2012 for SERC and 2013 for GPNA). The time after 3 PM was not considered because of the symmetry of the solar direction on the western side. Therefore, a total of 735 (unique combinations of 15 view2

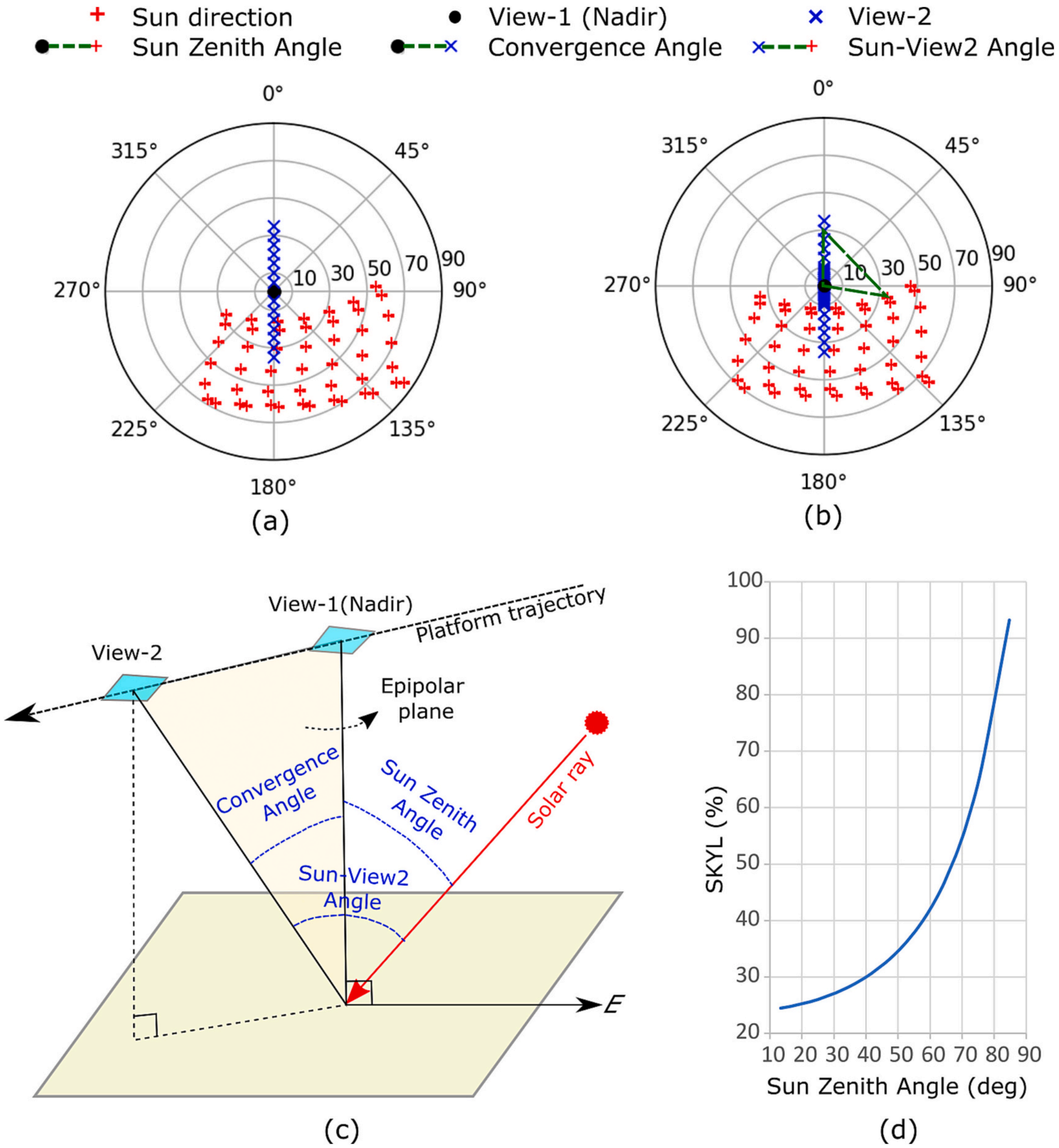

Fig. 2. Geometric and irradiance configurations of simulated along-track stereo pairs in this study. (a,b) Polar plot of the geometric configurations for the along-track stereogrammetry, including sun (red +), view1 (nadir, black circle), and view2 (off-nadir, blue x) for (a) SERC and (b) GPNA. (c) 3-D illustration of the directions and angles (sun zenith, convergence, and sun-view2), modified from Jeong and Kim (2016). (d) The SKYL (percentage of diffuse irradiance to the total irradiance) factor profile at the top of the canopy against various sun zenith angles. (For interpretation of the references to colour in this figure legend, the reader is referred to the web version of this article.)

angles × 7 h × 7 months) images for SERC and 1519 (31 × 7 × 7) images for GPNA with RPC models recorded in the metadata were simulated, as shown in Fig. 2. The configurations of the three variable directions (sun, view1, and view2) form a triangular pyramid. Our analyses are based on the three angles connected to the apex, which are defined and illustrated in Fig. 2. These three angles include:

1) The solar zenith angle (SZA, also the angle between the solar direction and view1 in our simulations) corresponds to the time of day and month at a specific location when the data were acquired.

The SZA at the summer solstice ranged from ~20° to ~ 60° over SERC, and from ~10° to ~ 50° over GPNA, while the SZA at the winter solstice varied from ~60° to ~ 85°over SERC and ~55° to ~ 80° over GPNA. When the view and sun directions are similar, the hotspot effect (enhanced image reflectance over vegetation due to reduced canopy and foliar shadow, e.g., Morton et al., 2014) can influence the observation of view1 (nadir) if the SZA is small. With predefined atmospheric configuration, the exponential relationship between the resultant SKYL (ranging from 25% at summer solstice noon for GPNA to 93% at winter solstice dawn/twilight for SERC) and all the SZAs used in the study are shown in Fig. 2d. The changing SKYL can influence the contrast of shadow textures over forests.

2) The Sun-View2 angle (SV2A) is the angle between the solar and view2 directions.

Similar to SZA, view2 is influenced by the hotspot effect if SV2A is small. In our simulation, the chance for view2 to be influenced by the hotspot effect is much larger than view1 because SV2A can extend from less than 5° to more than 100°.

3) The convergence angle (CA) is the angle between view1 and view2 (also the VZA of view2 in our simulations) along the epipolar plane.

The CA is directly related to the base-height ratio. Most existing data collected by stereo platforms have a relatively large along-track CA (e.g., the frequently used ~ 35° of WorldView constellations). However, Carl et al. (2013) and d'Angelo et al. (2014) suggested that a small CA with less occlusion from tri-stereo is more suitable for improving complex urban surface elevation retrieval with protruding high-rise urban buildings.

2.2.2. *Sensitivity study of other configurations*

Based on the sensitivity study of the three angles that influence acquisition geometry, we conducted two additional studies to explore the influence of the GSD of the two images in a stereopair and the geolocation offsets between the two views. Because of the expanding simulation volume, we studied only two to three instances of geolocation offset and GSD variation. In addition, the studies were conducted only over GPNA owing to the challenge of stereo reconstruction for the more complex shapes of the open canopy than those of the closed canopy.

2.2.2.1. GSD. The variation in GSD was achieved by downsampling the simulated images with 0.5 m GSD to 1.0 and 2.0 m for view1 and view2 through spatial averaging. We computed the RMSE' of DSM_{gen} for both homogeneous and mixed GSD (0.5 m view1 + 1.0 m view2; 1.0 m view1 + 2.0 m view2; 0.5 m view1 and 2.0 m view2) stereo combinations. These GSD combinations can be used to evaluate potential telescope and detector trades for future missions.

2.2.2.2. Geolocation offset. Geolocation offsets can occur in both the along- or cross-track acquisitions. To differentiate, we introduced two types of independent geolocation offsets between view1 and view2 to each axis of our simulated images: (1) within 1.0 m (averaged 0.5 m corresponding to expected ~1 pixel magnitude of linear pushbroom jitter artifacts), and (2) within 10.0 m (averaged 5.0 m corresponding to the expected magnitude of geolocation error for cross-track stereopairs acquired on different orbits). They are introduced as a constant offset to each control point location while generating the RPCs for each simulated image, which is a reasonable assumption for a small area of 16 ha and a short along-track distance of 400 m. In contrast, the effect over a longer along-track distance could become complicated with non-negligible piecewise replacement and image distortion (Wang et al., 2016).

3. Results

3.1. *Influences of geometric configurations*

3.1.1. *Closed canopy*

The influence of SZA, SV2A, and CA on $Bias_z$ and RMSE' over the closed forest site at SERC are shown by box-and-whisker plots (Langford, 2006) in Fig. 3. The overall height of the generated DSM (DSM_{gen}) was closer to DSM_{ref} than to DTM_{ref}, which is expected as there is little exposed terrain (Fig. 1). $Bias_z$ has a slight increasing trend from the negative to positive value range for all three angles, with both absolute median and interquartile range (IQR) values within 1.5 m. The RMSE' to DSM_{ref} does not have an obvious trend of the median (ranging from 2 to 3 m) and IQR for SZA and SV2A, as shown in Fig. 3ab. However, the median and IQR of RMSE' to DTM_{ref} decreased as the angles increased, which indicates that the DSM_{gen} became smoother with increasing angular offset between the sun and view directions.

In contrast, there is a clear trend in the RMSE' against DSM_{ref} with increasing CA (Fig. 3c). The median and IQR of the RMSE' distributions increase from (2.13 m, 0.16 m) to (3.01 m, 0.41 m) as CA increases, indicating that a smaller CA is preferable for generating a DSM of canopy height. This differs from the conventional recommendation of using a larger B/H ratio for better stereo reconstruction accuracy.

3.1.2. *Open canopy*

3.1.2.1. General results. The sensitivity study results for the open-canopy forest at GPNA are shown in Fig. 4. Both the value ranges and trends of the comparison results of the GPNA significantly differ from those of the closed-canopy forest at SERC. SZA and SV2A exhibit similar tendencies in $Bias_z$ and RMSE' due to a strong correlation, as shown in Fig. 4ab. For small angles, the $Bias_z$ is negative against DSM_{ref} and slightly positive against DTM_{ref}, indicating that the overall height of DSM_{gen} is closer to DTM_{ref} than to DSM_{ref}.As the SZA and SV2A increase, the $Bias_z$ against both the DTM_{ref} and DSM_{ref} rises until it intersects the median value of 0 against DSM_{ref} for SZA of $50-60°$ and SV2A of $60-70°$, where the overall height of DSM_{gen} is closer to DSM_{ref} than to DTM_{ref}. Compared to SV2A which does not show an obvious trend, the IQR consistently declines with increasing SZA (from 5.64 m to 1.21 m against DSM and from 5.56 m to 1.20 m against DTM), which indicates that the SZA is more sensitive compared to SV2A in controlling the IQR of $Bias_z$ in our simulated conditions. In contrast, RMSE' exhibits opposing trends for comparisons against the DTM_{ref} (increasing) and DSM_{ref} (decreasing) as both SZA and SV2A rise, and reaches the smallest RMSE' against DSM_{ref} for SZA of $50-70°$ (median: 4.98 m, IQR: 1.58 m) and SV2A of $60-70°$ (median: 4.33 m, IQR: 1.62 m). This trend co-varies with $Bias_z$, which intersects the median value of 0 against DSM_{ref} within approximately the same ranges of SZA and SV2A. Combining these results reveals that for small SZA and SV2A with a hotspot configuration, both the shape and height of DSM_{gen} are closer to DTM_{ref} than to DSM_{ref}, which is consistent with the validation results from the actual WorldView data (Yin et al., 2023). As both SZA and

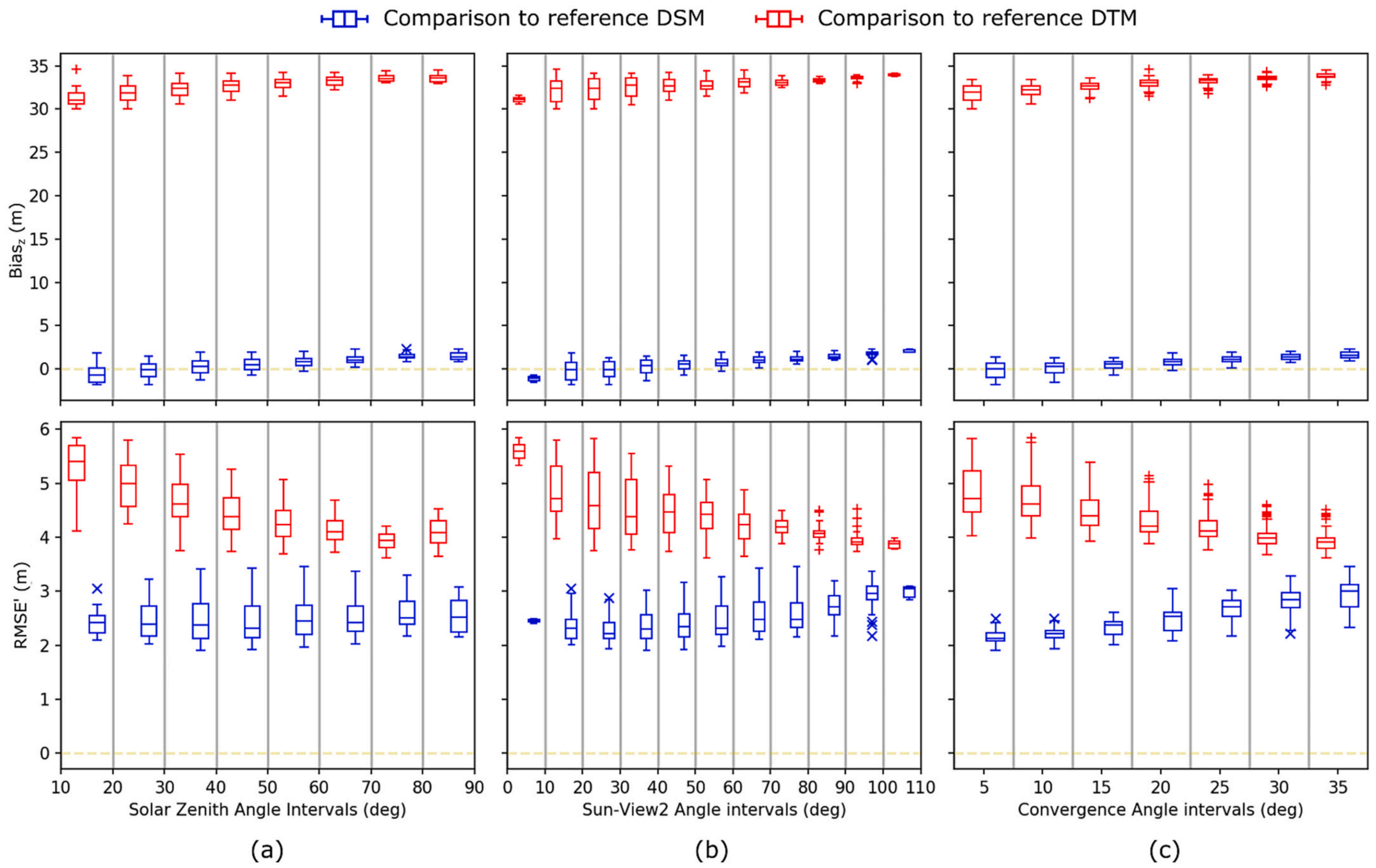

Fig. 3. Influence of SZA (a), SV2A (b), and CA (c) variations on vertical bias and RMSE' from the comparison between generated DSM from simulations (DSM_{gen}) against the reference DSM (blue boxes) and DTM (red boxes) over the SERC closed canopy. Each plot summarizes the along-track stereo combinations from 735 simulated image configurations. Within each bin, the comparisons against DSM_{ref} and DTM_{ref} are horizontally staggered to avoid overlapping, although both indicate the distribution within the same bin. (For interpretation of the references to colour in this figure legend, the reader is referred to the web version of this article.)

SV2A increase, the height of the DSM_{gen} becomes closer to the DSM_{ref}, yielding the best accuracy simultaneously.

The shaded relief maps prepared from the DSM_{gen} products illustrate the change in surface texture associated with different image acquisitions (Fig. 5). If SZA is small (closer to noon and the hotspot configuration), the DSM_{gen} is closer to the DTM_{ref}, with little texture variation associated with trees at the open-canopy forest site. As SZA increased, the best accuracy (lowest RMSE') was obtained for an SZA of 64° (SKYL: 47%), which corresponds to acquisitions in the early morning or late afternoon. Although DSM_{gen} textures corresponding to tree height can be observed, smearing artifacts obscure gaps between trees. Further increasing the SZA to 76° results in an additional reduction in accuracy and more smearing artifacts, because the strong diffuse insolation during dawn or twilight reduces the contrast from shadows (SKYL: 67%). Overall, enhancing accuracy by merely changing the SZA is relatively limited.

In contrast to the SZA and SV2A trends, the CA distribution for GPNA (Fig. 4c) generally exhibited a decreasing median $Bias_z$ against both DSM_{ref} and DTM_{ref}. The DSM_{gen} generated by a small CA ($< 10^\circ$) has an overall height close to the DSM_{ref} with a small IQR. It should be noted that the median of $Bias_z$ against the DSM_{ref} is always <0, indicating that the overall DSM_{gen} is always lower than the DSM_{ref}. In contrast, RMSE' median values exhibit an apparent asymptote distribution against DSM_{ref}, although the IQR increases with larger CA values. The optimal accuracy for the GPNA site occurs at 7° with an RMSE' median of 3.93 m and IQR of 0.33 m, much smaller than the typical $\sim 35^\circ$ CA of existing VHR satellites (median: 7.32 m, IQR: 1.27 m for 35° CA). The RMSE' values near 7° CA are similar for both the DSM_{ref} and DTM_{ref} comparisons, while the median RMSE' for the DTM_{ref} comparisons were generally smaller for both smaller and larger CA.

An optimal CA should balance the variation of VHR image texture matching from the anisotropic reflection of complex forest structures. It should be preferable in all aspects of DSM retrieval, including smaller median RMSE' and smaller IQR of the RMSE' compared against the DSM_{ref}. The CA for stereo surface generation substantially influences the definition of features over the open-canopy forest site at GPNA (Fig. 6). The results of small CA ($1^\circ, 3^\circ, 5^\circ, 7^\circ$, and 10°) used the geometric configurations shown in Fig. 4c, whereas those of large CA ($15^\circ, 20^\circ, 25^\circ, 30^\circ$, and 35°) used the geometric configurations shown in Fig. 2b. The CA with the smallest median $RMSE^{'}$ occurs at 7° (3.93 m). For CAs smaller than 7°, the DSM_{gen} images have blurred features, likely caused by more limited identification of reference textures between the different view directions with a fixed 0.5 m GSD, for which the textures may only be distinguishable at the sub-pixel scale. At 7° CA, the structure of pine trees of different heights was more comparable to the DSM_{ref} image (Fig. 1b). As the CA increases, the DSM_{gen} is also smeared, but larger CAs tend to emphasize the terrain surface instead of the vegetation features. Indeed, the features of the highly protruding crown structures of old pines vanished from the DSM_{gen} images, which is consistent with the stereo surfaces derived from actual WorldView data with larger CAs (Yin et al., 2023). Given the overall relationship of increasing RMSE' with larger CAs, the frequently used $\sim 35^\circ$ CA of the existing WorldView stereo products is not an optimal configuration for capturing the canopy shape distribution. By contrast, larger CAs are suitable for bare terrain stereo reconstructions, especially for areas with limited slopes and relief (simulation results shown in Appendix B),

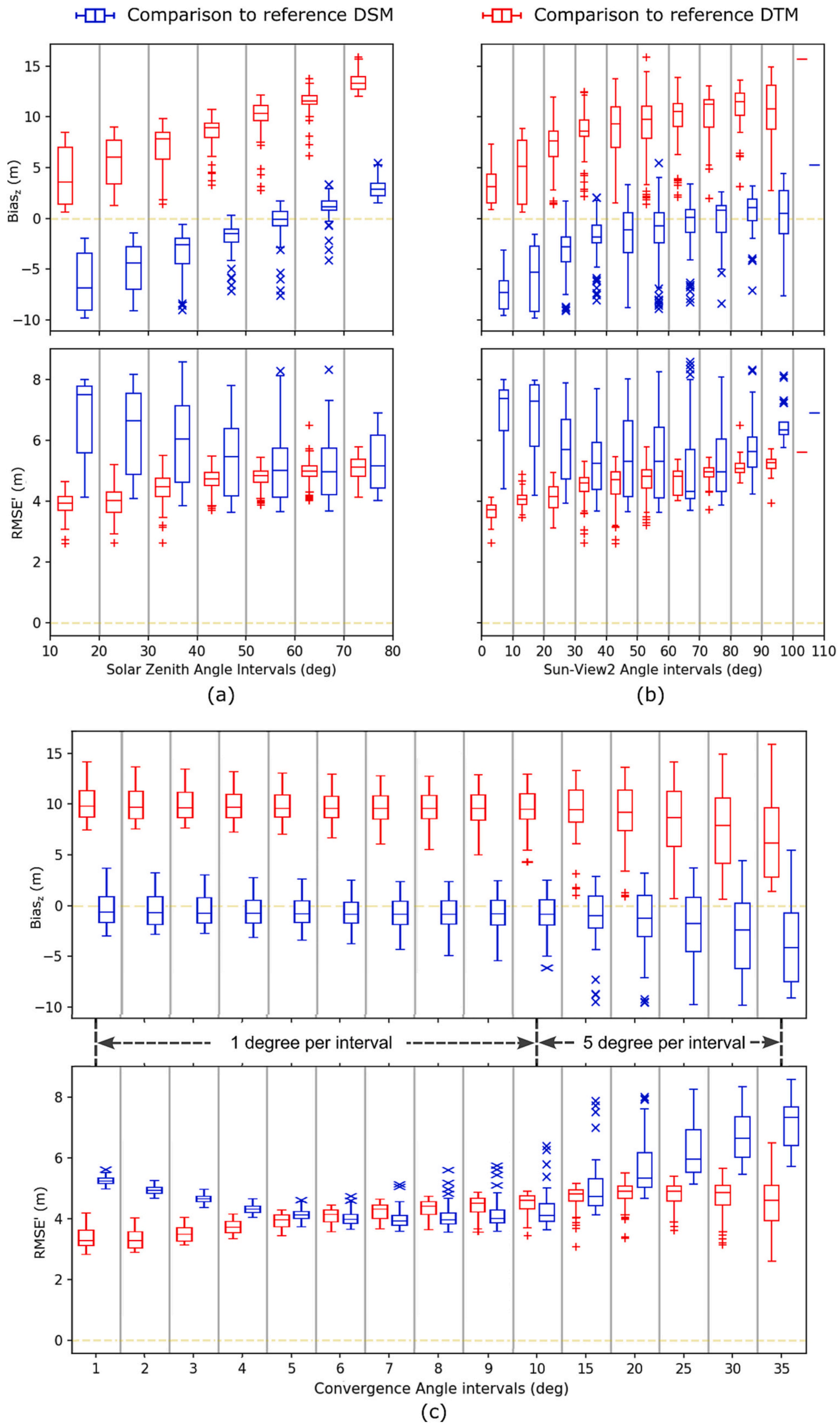

Fig. 4. Influence of SZA (a), SV2A (b), and CA (c) variations on vertical bias and RMSE' from the comparison between DSM_{gen} against the reference DSM and DTM at GPNA (open canopy). (a) and (b) summarize the along-track stereo combinations from 735 simulated image configurations (5-degree VZA step), while (c) summarizes the combinations of 1519 simulated images with 1-degree CA step (from 1 to 10 degrees) and 5-degree CA step (from 10 to 35 degrees).

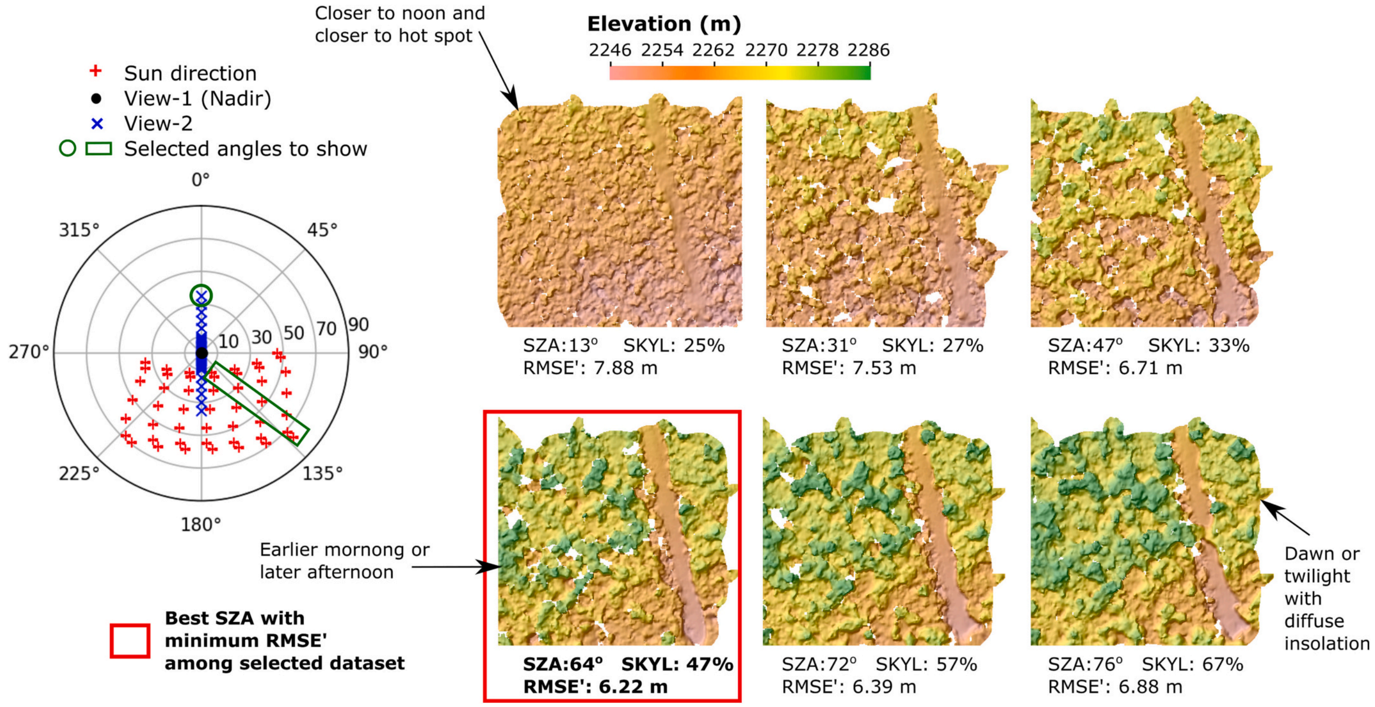

Fig. 5. Sample of generated DSMs with associated RMSE' (to DSM_{ref}) for stereopairs with different SZA over GPNA. For the selected simulations, the *CA* is fixed at 35° (viewing from the south), and the selected dates and times capture a small variation range in the solar azimuth angle. The best SZA (64°, SKYL: 47%, 8 AM local on 20 October 2013) among the selected datasets is outlined in red, with an $RMSE' = 6.22\ m$. (For interpretation of the references to colour in this figure legend, the reader is referred to the web version of this article.)

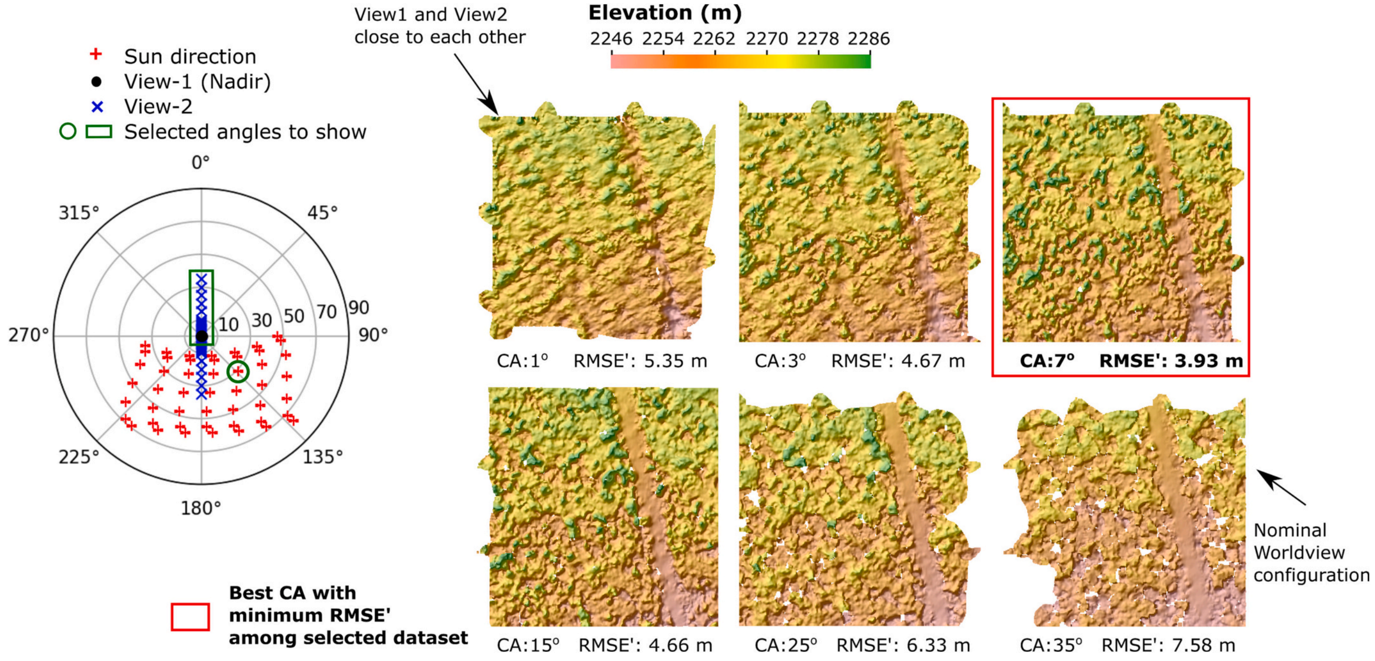

Fig. 6. Influence of convergence angle (CA) on DSM accuracy, measured as RMSE' relative to DSM_{ref} for GPNA. Sample simulations had fixed time (8 AM local 20 June 2013, $SZA = 46.42°$, $SKYL = 33\%$) and view azimuth angle (180°, from south). The DSM with the lowest RMSE' (3.93 m) had a CA of 7° (red outline). (For interpretation of the references to colour in this figure legend, the reader is referred to the web version of this article.)

which is consistent with the conventional recommendation of larger B/H ratios. Additional discussions of CA recommendations for forest and bare terrain are presented in Section 4.1.

3.1.2.2. Influence of the spatial pattern of vegetation on the differences in canopy surface estimates. The differences in canopy surface elevation between the co-registered DSM and reference DSM ($DSM_{cr} - DSM_{ref}$) display important variations in characterizing fine-scale details in forest structure (Fig. 7). For stereopairs with an oblique SZA and a large CA (Fig. 7a and Fig. 5), the surface model underestimates the height of the tallest trees (old pines) due to the loss of matching features in the stereo imagery, while the heights of trees in the lower canopies are

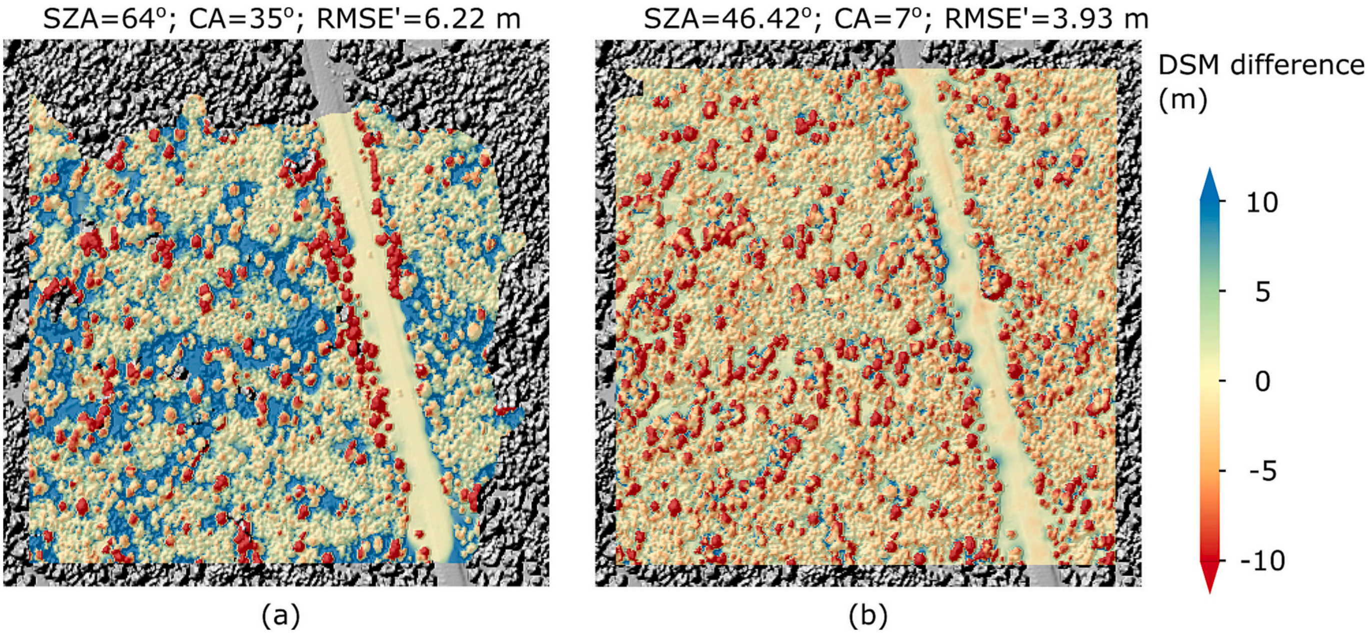

Fig. 7. Difference maps ($DSM_{cr} - DSM_{ref}$) computed from the two DSM_{gen} examples with the best accuracy for the open forest site at GPNA (red outlines in Fig. 5 and 6) illustrating the influence of (a) SZA and (b) CA on fine-scale details in forest structure. (For interpretation of the references to colour in this figure legend, the reader is referred to the web version of this article.)

overestimated due to occlusion. Both effects contribute to the appearance of smearing in the DSMs with a large CA. Stereopairs with small CA (Fig. 7b and Fig. 6) mitigate both effects. Height and cover heterogeneity at the GPNA site result in a prevailing difference pattern in the DSM with a small CA, where overestimates are common along the forest edges and underestimates align with the tallest trees. The open canopy structure at GPNA is more challenging to accurately capture with stereo-derived surfaces than more homogenous forest sites with closed canopy, such as SERC (see Section 3.1.1).

3.2. *Influence of ground sampling distance (GSD)*

We examined the influence of GSD, on the accuracy of DSM_{gen} at GPNA, the more complex site for stereogrammetry. Overall, the RMSE' increases as the GSD of the imagery for stereo reconstruction increases from 0.5 to 2.0 m (Fig. 8). As the GSD increases, the optimal CA bin containing the global minimum of the asymptote also increases, that is, the 5° bin for 0.5 m GSD (median: 4.12 m, IQR: 0.23 m), the 10° bin for 1.0 m GSD (median: 4.95 m, IQR: 0.40 m), and the 15° bin for 2.0 m GSD (median: 6.34 m, IQR: 0.54 m). In general, a smaller GSD exhibits better accuracy against the DSM_{ref}, with the exception of the results for a large CA (the 35° bin), which has a similar median value but a reduced IQR as GSD increases. The RMSE' against DTM_{ref} is reduced as GSD increases, suggesting that larger GSD generates a smoother surface due to the smearing effect for open forests.

The accuracy of the DSMs generated from mixed GSD images was intermediate compared to cases with homogeneous GSD for both images in the stereopair (Fig. 8b). These cases correspond to a configuration with a smaller GSD in the nadir view and a larger GSD in the oblique view. For rig stereo instruments, such configurations could reduce the size, weight and power of the off-nadir telescope, which impacts mission cost and complexity. In general, the accuracy of the mixed cases was closer to that of the smaller homogeneous GSD (which also has a smaller RMSE') than the larger homogeneous GSD. Results based on RMSE' were consistent with the differences in DSM_{gen} from the mixed GSD against each homogeneous GSD. Additionally, the 0.5 m view1 + 2.0 m view2 GSD produces a median accuracy trend close to 1.0 m homogeneous GSD accuracy.

3.3. *Influence of geolocation offsets*

We examined the influence of geolocation offsets on the accuracy of the DSM_{gen} for the GPNA site (Fig. 9). We assigned the possible along-track (pushbroom jitter) and cross-track (between separate orbits) axial offsets with averages of 0.5 and 5.0 m for each stereopair, respectively. The geolocation offset results in no apparent change in the median $Bias_z$. However, the IQRs of $Bias_z$ do increase as a result of geolocation offsets, especially for smaller CAs. Geolocation offsets did not introduce apparent impacts on the RMSE', regardless of the offset. Therefore, a geolocation offset, which is assumed to be consistent across a small scene, mainly causes an offset in the generated DSM. The potential approaches for bias corrections, including the conditions of a larger area and a longer along-track distance, are discussed in Section 4.3.

4. Discussions and conclusions

This sensitivity study evaluated the optimal acquisition configurations for retrieving surface models over open and closed-canopy forests using DART-simulated VHR stereopairs. We found that, without a steep topography, a more oblique SZA ($50-70°$) and smaller CA ($<35°$, optimal angles varied depending on GSD) provided better accuracy for retrieval of the forest canopy surface. These findings are broadly consistent with previous research, e.g., the optimal SZA from 55° to 65° suggested by Montesano et al. (2017) and the fact that the DSM accuracy of a small CA of 12° outperformed that of a larger CA of ~ 25° (Piermattei et al., 2018). In addition, the simulation methods can consider a broader range of image acquisition conditions in the model environment, compared to the actual VHR stereo data with limited configurations. Stereopairs with a hotspot configuration generated elevations close to the DTM for open forests, which is consistent with the WorldView data over GPNA as demonstrated in (Yin et al., 2023). In general, smaller GSD improved the accuracy of the DSM for simulations with the same geometric configurations. In addition, for small areas, a consistent geolocation offset between the two simulated images of a stereopair mainly induced a vertical bias in the generated DSM without apparent influence on accuracy (RMSE' estimated after co-registration).

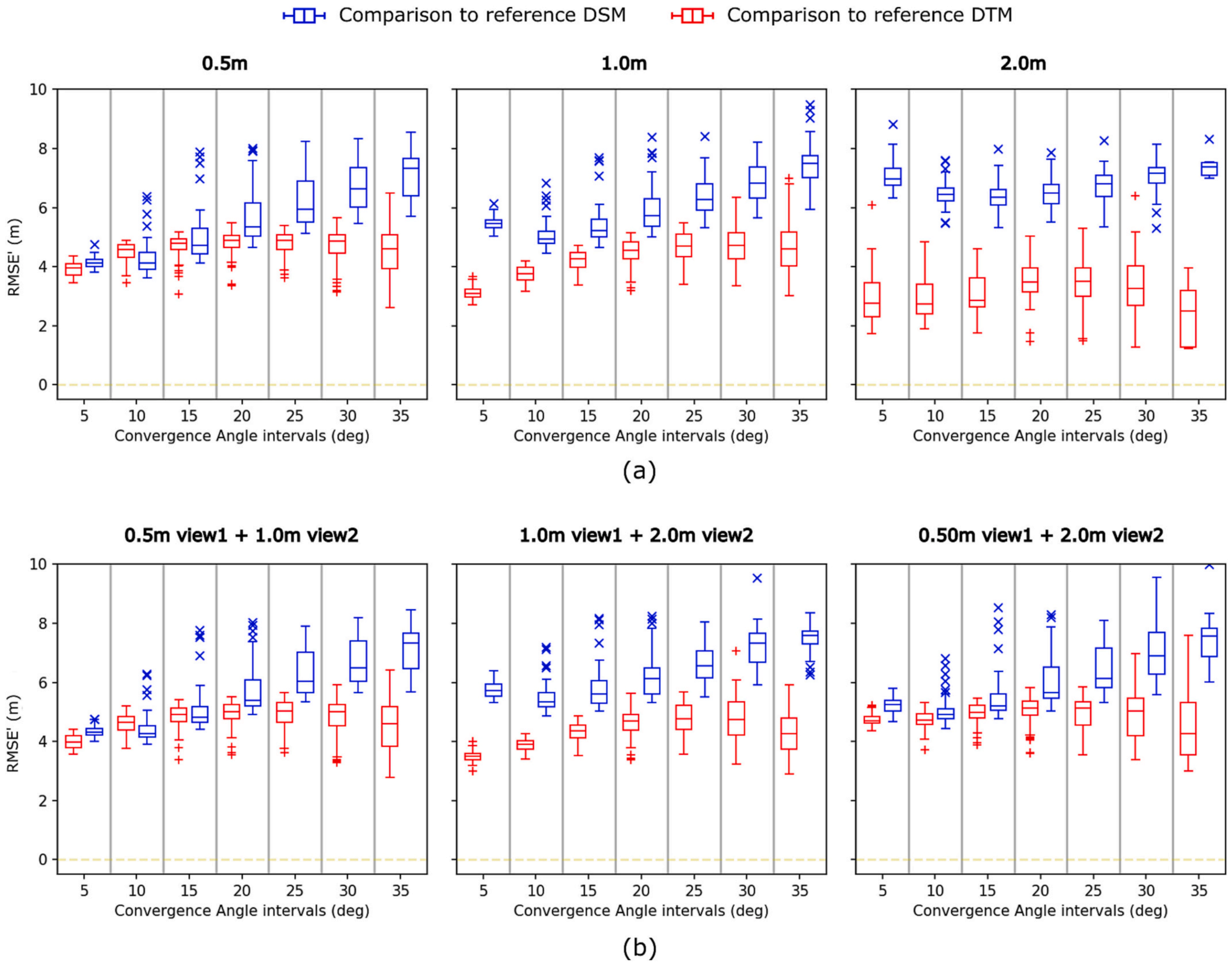

Fig. 8. Influence of increasing ground sampling distance (GSD) from 0.5 to 2.0 m on the RMSE' of the generated DSM against the reference DSM for a range of convergence angles at GPNA. (a) RMSE' of generated DSMs from images with homogeneous GSD for both view1 and view2 (b) RMSE' of generated DSMs from images with mixed GSD for view1 and view2.

These results are significant for several reasons. First, they provide a benchmark for conducting further analyses or developing stereo processing algorithms for canopy surface elevations. Second, these results and the developed tools provide guidance for future VHR satellite acquisition strategies that focus on capturing vegetation structure, given the broad interest in the potential use of stereogrammetry for the surface topography and vegetation targeted observable identified in the 2017 Decadal Survey (NASA, 2021). Finally, these results suggest that currently available regional mosaics of VHR stereo DSM products (e.g., ArcticDEM, etc.) prepared from DSM strips with a range of acquisition configurations likely have spatially variable accuracy for canopy surface elevations. Further analyses of the optimal configurations and requirements of stereogrammetry for forest canopy structure retrieval are discussed below.

4.1. Optimal geometric configurations for along-track stereogrammetry over forests

To optimize the accuracy of vegetation surface elevation estimates, we recommend a set of stereo configurations that differ from those initially adopted for general-purpose applications without a focus on vegetation. Our study confirms the conventional approach for optimizing accuracy with a larger B/H ratio for stereo reconstruction over exposed surfaces, as shown in Fig. A 1c (Appendix B). In addition, a large CA induces less vertical bias generated by geolocation offsets, and a negligible influence is observed for 35° (see Fig. 9). Therefore, a relatively large CA is appropriate for stereo reconstruction of relatively flat surfaces with limited slopes.

However, for forests, a smaller CA yields better accuracy. This is consistent with the findings of Piermattei et al. (2018): a small CA of 12° from the tri-stereo configuration of Pléiades-HR (0.5 m resolution) was found to be favorable in terms of accuracy and completeness of forest canopy shape, compared to the CA of ∼ 25° of another dataset. Owing to the tri-stereo property of Pléiades, the forward-nadir and backward-nadir CA of ∼ 5° generated less accurate results compared to the forward-backward CA of 12°, which is also partially consistent with our simulation results. Indeed, 5° and 12°are distributed on the opposite sides of the global minimum of the optimal CA for the VHR stereo of 0.5 m GSD. However, the optimal CA for Pléiades may not be the same as the optimal CA derived from our paired simulation results, because the resolution is not conceptually equivalent to GSD and the optimal CA varies with different GSD. Nevertheless, it is essential to note that CAs larger than the optimal value increase the RMSE' from the simulation results. Therefore, the selection of any CA between the optimal value and a larger CA boundary at 35°, for example, can persistently generate

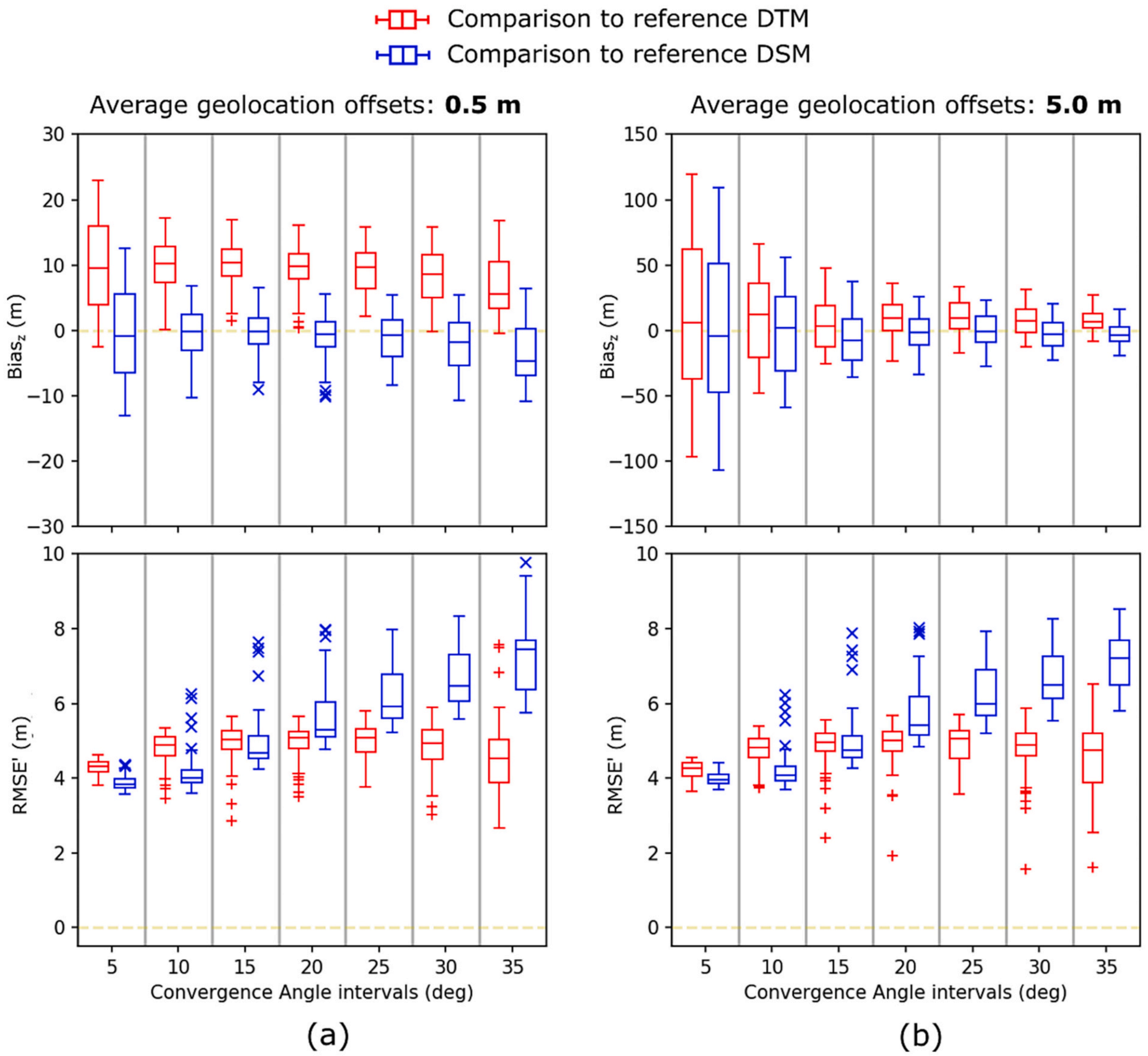

Fig. 9. Influence of axial geolocation offsets with averages of 0.5 m (a) and 5.0 m (b) on the vertical bias and *RMSE*$'$ of DSMs for the GPNA site for different CAs.

better results than a CA of 35°. This finding offers guidance to support future stereo mission design and operations to improve the stereo-generated DSM accuracy over forests. Furthermore, commercial VHR satellite vendors should consider offering smaller along-track stereo CA in their standard data acquisition modes. The modeling framework also provides a flexible environment for further study of potential design factors or sensor attributes, such as an additional study to account for the effect of light diffraction and geolocation errors due to linescan jitter across a larger area.

Combining all the simulation results shown in Fig. 4 indicates that CA is the most critical variable of the geometric configuration for stereo image acquisition over a small area in open forests. Ideally, the accuracy of the DSM from stereogrammetry should approach that derived from small-footprint airborne lidar. Compared to the RMSE' for the optimal SZA of 50 – 70° (median: 4.98 m, IQR: 1.58 m), the RMSE' of the optimal CA of 7° showed apparent advantages in terms of higher accuracy and stability (median: 3.93 m, IQR of 0.33). In addition, oblique SZA is known to be limited by steep topography in mountainous areas (Ni et al., 2019, 2023), while the control of CA can be relatively flexible for most of the existing VHR satellite missions.

4.2. *Convergence angle influence on generated DSMs: the tradeoff between height accuracy and completeness*

The vegetation canopy shape, height, density and overall arrangement on the landscape are important factors in the accuracy of canopy surface estimates from stereogrammetry. Considering the similar structural complexity of protruding shapes between high-rise urban buildings and forest trees, similar suggestions for small CA stereopairs can be found in past work on urban infrastructure height retrieval (Carl et al., 2013; d'Angelo et al., 2014). In addition, the DSM accuracy relies on the reconstruction algorithms, evaluation criteria, and quality of reference datasets. However, occlusions induced by a large CA for two-image stereo can not be easily corrected using traditional stereo processing algorithms, although a systematic evaluation of available algorithm performance as a function of CA is an important area for future study. It was found that although different algorithms play a specific role in stereo reconstruction, the geometric configuration is still the decisive factor affecting the final results (Qin, 2019; Albanwan and Qin, 2022).

For forests, in addition to the occlusion caused by complex canopy shapes, the bidirectional reflectance variation further reduces the number of matched points from a stereopair, requiring an even smaller view angle difference to reconstruct the shape compared to the reduced anisotropic property of the urban building surface. In addition, the mass-processing workflow used by ADAPT (i.e., the ASP SGM algorithm) tends to fill gaps (personal communication with Oleg Alexandrov). These factors lead to a tradeoff between 1) accurate absolute height retrieval with more data gaps due to occlusions (large CA) and 2) less accurate, but more complete forest surfaces (small CA). Therefore, the fundamental consideration of stereogrammetry application in complex landscape structures (such as forests or urban infrastructure) is the choice of the two tradeoff options for different objectives.

The current global archive of VHR stereopairs from WorldView features primarily larger CA. For open forests, the total range of RMSE' between whiskers for the sensitivity study of 35° CA is about 2.85 m, which is similar to the ∼2 m RMSE range reported by Montesano et al. (2017) across Boreal forests. In addition, although we are working on forested landscapes, the analogy can apply to dense, high-rise buildings in urban landscapes. Qin (2019) showed that, over such areas, the RMSE' ranges from ∼6 m to ∼10 m (∼4 m between the largest and smallest values) for 35° CA. This magnitude of accuracy is potentially tenable in the case of urban applications where estimated heights are typically assigned to polygons defining building outlines created through a land survey. Therefore, a few matched points retrieved from the top of a building can provide sufficient height information with high accuracy, although occlusions persist. In contrast, we do not have data on the location and crown extent of the three trillion trees on Earth, and the absolute heights of a limited number of matched points do not have a clear advantage over other technologies, such as lidar. Our study strongly supports using a smaller CA to reconstruct stereo surface elevations over forests. Some existing images captured by the tri-stereo configuration of Pléiades with smaller CA can potentially provide a better forest DSM reconstruction.

4.3. Minimizing the canopy surface biases derived from small convergence angles and geolocation offsets

Stereogrammetry from pairs with small convergence angles provides important coverage of canopy gaps, but involves a tradeoff of increased vertical bias compounded by the geolocation offsets. Although the replacement and image distortion induced by jitter could be corrected by using high-accuracy and high-frequency attitude data as reported for the ZY-3 satellite (Wang et al., 2016), it is questionable whether the jitter correction approach can be universal to all existing VHR satellites with various sensor/platform configurations and data quality. Alternatively, data from a potential multi-sensor platform or cross-platform fusion should be investigated to minimize the derived canopy surface biases.

From the simulation results over small study areas, considerable IQR of vertical bias was identified for random geolocation offsets with an average of 0.5 m along each axis, corresponding to pushbroom jitter, especially for the small CA configuration suggested above. The IQR was further amplified for 5 m offsets. The fact that the RMSE' profile remains the same regardless of the geolocation offset indicates that additional processing should focus on vertical bias correction. A traditional method is to use an existing reference DSM to rectify the vertical bias towards the same elevation, given that the reference DSM is sufficiently accurate. Point cloud co-registration methods can also be used to fit 3D combinations of translation, rotation, and scaling transformations to observed residual offsets between point clouds, such as the iterative closest point (ICP) implementation in ASP (Pomerleau et al., 2013). However, forest surfaces present challenges for accurate DSM alignment because of the lack of large-scale accurate DSM over forests and real offsets between the true "first-return" surface from airborne lidar and the lower surface from stereo reconstruction. Therefore, the alignment to resolve the vertical bias induced by small CA can be coarse based on the existing forest DSM globally, which was mostly derived from stereogrammetry of a large CA with lower resolutions of past platforms.

The fusion of stereo DSMs with spaceborne lidar can potentially mitigate the vertical bias induced by a small CA. Indeed, lidar returns within the swath of VHR images can be considered as "nails" that pin the "canvas" of stereo DSM onto its accurate 3-D position. A lidar waveform can parse the forest structure within its footprint into the highest canopy elevation, terrain elevation, and, to a lesser extent, tree height distribution. Matching this information with a stereo-generated DSM within the lidar footprint could provide a reference elevation for vertical bias correction and potentially more complex alignment transformations of the DSM to mitigate the underestimation and improve accuracy. In addition, stereogrammetry over forests provides complementary information on high-resolution canopy shape distribution that sparse laser altimetry data from satellites currently cannot deliver. The fusion of the complementary products of lidar and stereogrammetry can potentially improve global forest information retrieval, such as the clumping effect correction to a certain extent to better estimate LAI (Jiang et al., 2021). These two technologies are under consideration for future NASA missions targeting the Surface Topography and Vegetation observable (NASA, 2021). We are currently performing additional simulations for combined stereo and lidar (Gastellu-Etchegorry et al., 2016; Wei et al., 2020; Yin et al., 2013, 2016, 2020; Yang et al., 2022) instrument trades at the SERC and GPNA test sites used in this study.

4.4. DTM estimation of the open forest using stereopairs with a hotspot configuration

DeWitt et al. (2017) reported that the DTM of deciduous open forests could be estimated by filtering the leaf-off stereo-derived DSM. Here, we found that, over open forests with leaf-on conditions, VHR stereopairs containing images with hotspot configuration can be used to derive an elevation that more closely matches the DTM. This is confirmed by both actual WorldView acquisitions over GPNA (Yin et al., 2023), and the sensitivity study of solar direction conducted in Section 3.1.2. Indeed, the hotspot effect over one VHR image of a stereopair causes the loss of shadow textures from both the crown shape and leaves, generating considerable diversity in the crown reflectance and the proportion of shadows compared to the other VHR image without hotspot effect. In contrast, the ground reflectance and textures are much less influenced by the solar incident direction. In that case, more textures can be matched over the ground than the forest canopy. This finding is promising for a potential application of VHR stereogrammetry over boreal forests to estimate the canopy height and biomass, by subtracting a filtered hotspot-derived DSM (e.g., as illustrated in SZA:13 of Fig. 5) from a DSM derived from small CA (e.g., as illustrated in CA:7 of Fig. 6).

4.5. Simulation advantages and limitations

Although we simulated and analyzed thousands of configurations in VHR stereogrammetry, three aspects cause the major differences between DART-simulated images and the actual images: 1) the cubic voxel shape spanning over different pixels after projection along the view direction; 2) the unknown point-spread function which describes the diffraction of light on the sensor plane (Kolb et al., 2016); and 3) the variable sub-pixel image artifacts caused by linescan pointing error (jitter) (Tong et al., 2014), which was neglected because of our small study areas. The observed RMSE' differences between DSMs derived from simulation and actual data (Yin et al., 2023) could add small margins to our sensitivity study results (0.17 m for SERC, 0.21 and 0.72 m for GPNA). DART will be enhanced to eliminate or mitigate these aspects in a future release. In addition, the default aerosol model of 23 km RURAL visibility could be different from reality. Furthermore, the simulations for these study sites (∼400 m) are small compared to the larger swath dimensions of many linescan stereo datasets (∼10–20 km wide, ∼15–110 km long). This could be solved by adapting to the latest DART-Lux implementations (Wang et al., 2022), which have less memory usage to allow a larger scene. Also, the study areas have small slopes, and the topography can impact the stereo reconstruction. This will be studied in the future by selecting a mountainous study area with G-LiHT data coverage.

This study also showed many advantages of combining PVlad with DART. The forest scenes were physically reconstructed in the 3-D distribution of LAD derived from airborne lidar point reflectance using PVlad. Forward modeling of the physical DART model was executed to simulate remote sensing images close to reality. In addition to the sensitivity study, this approach can build high-fidelity realistic training data using a deep learning approach for information retrieval and testing interdisciplinary image processing and computer vision algorithms. The abundant G-LiHT data across the USA provides a considerable number of potential scenes to create realistic data from the simulations.

Open access to the simulated data

For both SERC and GPNA, the simulated VHR images with RPC stored in GeoTIFF format and the reference DSM/DTM used in this study can be openly accessed from https://glihtdata.gsfc.nasa.gov/files/tmp/StereoModeling/.

CRediT authorship contribution statement

Tiangang Yin: Conceptualization, Methodology, Software, Writing – original draft, Investigation, Validation, Writing – review & editing. **Paul M. Montesano:** Methodology, Software, Writing – original draft, Investigation, Data curation. **Bruce D. Cook:** Data curation, Investigation, Methodology, Supervision, Writing – review & editing. **Eric Chavanon:** Methodology, Software, Visualization, Validation. **Christopher S.R. Neigh:** Conceptualization, Methodology, Software, Supervision, Writing – review & editing. **David Shean:** Conceptualization, Methodology, Software, Writing – review & editing. **Dongju Peng:** Methodology, Software, Investigation. **Nicolas Lauret:** Methodology, Software, Investigation. **Ameni Mkaouar:** Investigation, Validation, Writing – review & editing. **Omar Regaieg:** Methodology, Investigation, Validation. **Zhijun Zhen:** Methodology, Investigation, Validation. **Rongjun Qin:** Software, Validation, Writing – review & editing. **Jean-Philippe Gastellu-Etchegorry:** Conceptualization, Software, Investigation, Supervision. **Douglas C. Morton:** Conceptualization, Investigation, Supervision, Writing – original draft, Writing – review & editing.

Declaration of Competing Interest

The authors declare that they have no known competing financial interests or personal relationships that could have appeared to influence the work reported in this paper.

Model availability

The functionalities used in this work have been implemented in the latest release of the DART model. DART provides free licenses for research and education purposes (https://dart.omp.eu/).

Acknowledgments

This research was supported by (1) NASA Goddard Space Flight Center's Internal Research and Development Program (2) NASA's Commercial SmallSat Data Acquisition Program (CSDA) augmentation to the Terrestrial Ecology Program [grant number NNH16ZDA001N-CARBON] and (3) NASA's Earth Science Technology Office [grant number NNH21ZDA001N-DSI]. Maxar data were provided by NASA's Commercial Archive Data for NASA investigators under the National Geospatial-Intelligence Agency's NextView license agreement. The authors are also thankful to Guoqing Sun at the University of Maryland and Oleg Alexandrov at NASA Ames Research Center for their valuable suggestions. The authors also thank the anonymous reviewers for their valuable suggestions.

Appendix A. VHR satellite platforms

Table A.1
The List of VHR satellites with stereo capability, partially retrieved from Deilami and Hashim (2011).

Satellite Name	Country	Company/Institute	Launch Date	Best Stereo Resolution (m)
Cartosat constellation	India	ISRO[a]	2005–2019	0.25
Deimos-2	Spain	Deimos Imaging	June 19, 2014	1.00
DubaiSat-2	United Arab Emirates	MBRSC[b]	November 21, 2013	1.00
EROS-A1	Israel	ImageSat International	December 5, 2000	1.80
EROS-B1	Israel	ImageSat International	April 25, 2006	0.70
Gaofen-7	China	CAST[c]	November 3, 2019	0.50
GeoEye-1	USA	Maxar	September 6, 2008	0.41
IKONOS	USA	Maxar	September 24, 1999	0.82
KOMPSAT-2	South Korea	KARI[d]	July 28, 2006	1.00
KOMPSAT-3	South Korea	KARI	May 17, 2012	0.55
Kompsat-3 A	South Korea	KARI	March 25, 2015	0.55
Pléiades-HR 1 A	France	Airbus	December 17, 2011	0.50
Pléiades-HR 1B	France	Airbus	December 2, 2012	0.50
QuickBird	USA	Maxar	October 18, 2001	0.65
SkySat constellation	USA	Planet	2016–2020	0.70
SPOT 6	France	Airbus	September 9, 2012	1.50
SPOT 7	France	Airbus	June 30, 2014	1.50
TripleSat-1	China	21AT[e]	July 10, 2015	0.80
TripleSat-2	China	21AT	November 21, 2018	0.80
TripleSat-3	China	21AT	December 3, 2018	0.80
WorldView-1	USA	Maxar	September 18, 2007	0.50
WorldView-2	USA	Maxar	October 8, 2009	0.46
WorldView-3	USA	Maxar	August 13, 2014	0.31
WorldView-4	USA	Maxar	November 11, 2016	0.31
ZY-3	China	CAST	January 9, 2012	2.10

[a] ISRO – Indian Space Research Organisation.
[b] MBRSC – Mohammed Bin Rashid Space Centre.
[c] CAST – China Association for Science and Technology.
[d] KARI – Korea Aerospace Research Institute.

[e] 21AT – Twenty First Century Aerospace Technology Pte. Ltd.

Appendix B. Bare-earth simulations over GPNA

As shown in Fig. A.1, only DTM_{ref} of GPNA was used for comparison because forest features do not exist in the simulated scene. For $Bias_z$, the trends of all the three angles are observed to move from a small positive to small negative median within 0.05 m. Although the IQR of $Bias_z$ can reach 0.10 m for small SZA and CA, it is much reduced for larger angles. The RMSE' trend is apparent for both SZA and CA, with a reduction in the median and IQR for the rising angles. Although a larger SZA provides better accuracy, the influence of the hotspot effect is much less than that of the closed (Fig. 3a) and open (Fig. 4a) forest scenarios. The effect of CA on accuracy is predominant over other angles, and the RMSE' reaches a median of 0.17 m and IQR of 0.13 m for CA of 35°.

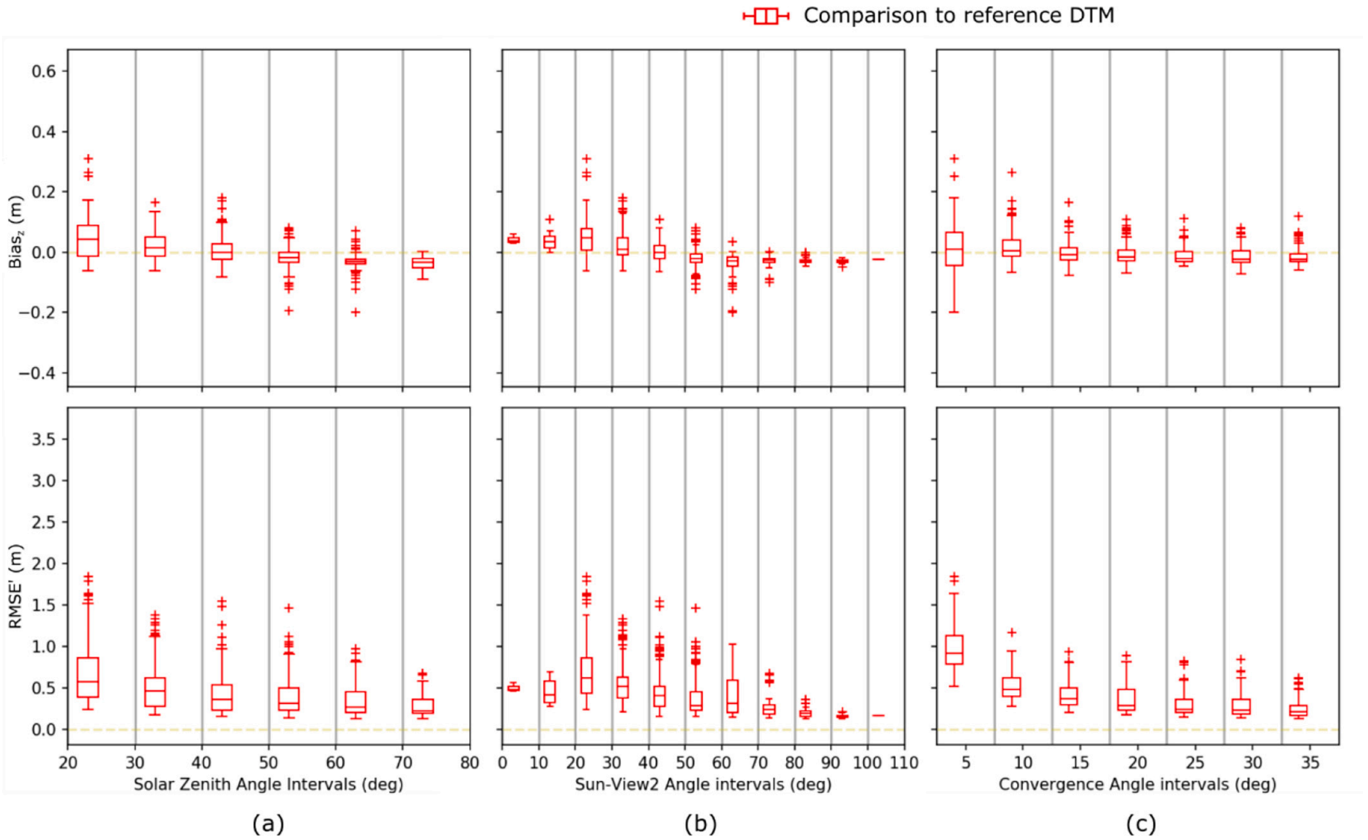

Fig. A.1. Influence of SZA (a), SV2A (b), and CA (c) variations on vertical bias and RMSE' by comparing generated DSM against the reference DTM over the bare-earth scene of GPNA (reference DTM shown in Fig. 1b; geometric configurations shown in Fig. 2b).

References

Abdalati, W., Zwally, H.J., Bindschadler, R., Csatho, B., Farrell, S.L., Fricker, H.A., Harding, D., Kwok, R., Lefsky, M., Markus, T., Marshak, A., Neumann, T., Palm, S., Schutz, B., Smith, B., Spinhirne, J., Webb, C., 2010. The ICESat-2 laser altimetry mission. In: Proceedings of the IEEE, 98, pp. 735–751.

Albanwan, H., Qin, R., 2022. A comparative study on deep-learning methods for dense image matching of multi-angle and multi-date remote sensing stereo-images. Photogramm. Rec. 37, 385–409.

Berk, A., Bernstein, L.S., Robertson, D.C., 1987. MODTRAN: A moderate resolution model for LOWTRAN. Spectral Sciences Inc, Burlington MA.

Berthier, E., Floriciou, D., Gardner, A.S., Gourmelen, N., Jakob, L., Paul, F., Treichler, D., Wouters, B., Belart, J.M.C., Dehecq, A., Dussaillant, I., Hugonnet, R., Kääb, A., Krieger, L., Pálsson, F., Zemp, M., 2023. Measuring glacier mass changes from space—a review. Rep. Prog. Phys. 86, 036801.

Beyer, R.A., Alexandrov, O., McMichael, S., 2018. The Ames stereo pipeline: NASA's open source software for deriving and processing terrain data. Earth Space Sci. 5, 537–548.

Bhushan, S., Shean, D., Alexandrov, O., Henderson, S., 2021. Automated digital elevation model (DEM) generation from very-high-resolution planet SkySat triplet stereo and video imagery. ISPRS J. Photogramm. Remote Sens. 173, 151–165.

Bolch, T., Pieczonka, T., Benn, D.I., 2011. Multi-decadal mass loss of glaciers in the Everest area (Nepal Himalaya) derived from stereo imagery. Cryosphere 5, 349–358.

Bosch, M., Kurtz, Z., Hagstrom, S., Brown, M., 2016. A multiple view stereo benchmark for satellite imagery. In: 2016 IEEE Applied Imagery Pattern Recognition Workshop (AIPR), pp. 1–9.

Bruening, J., Fischer, R., Bohn, F., Armston, J., Armstrong, A., Knapp, N., Tang, H., Huth, A., Dubayah, R., 2021. Challenges to aboveground biomass prediction from waveform lidar. Environ. Res. Lett. 16.

Carl, S., Bärisch, S., Lang, F., d'Angelo, P., Arefi, H., Reinartz, P., 2013. Operational generation of high-resolution digital surface models from commercial tri-stereo satellite data. In: Photogrammetric Week'13, pp. 261–269.

Cook, B., Corp, L., Nelson, R., Middleton, E., Morton, D., McCorkel, J., Masek, J., Ranson, K., Ly, V., Montesano, P., 2013. NASA Goddard's LiDAR, hyperspectral and thermal (G-LiHT) airborne imager. Remote Sens. 5, 4045.

d'Angelo, P., Rossi, C., Minet, C., Eineder, M., Flory, M., Niemeyer, I., 2014. High resolution 3D earth observation data analysis for safeguards activities. In: Symposium on International Safeguards, pp. 1–8.

Deilami, K., Hashim, M., 2011. Very high resolution optical satellites for DEM generation: a review. Eur. J. Sci. Res. 49, 542–554.

DeWitt, J.D., Warner, T.A., Chirico, P.G., Bergstresser, S.E., 2017. Creating high-resolution bare-earth digital elevation models (DEMs) from stereo imagery in an area of densely vegetated deciduous forest using combinations of procedures designed for lidar point cloud filtering. GISci. Remote Sens. 54, 552–572.

Dubayah, R., Blair, J.B., Goetz, S., Fatoyinbo, L., Hansen, M., Healey, S., Hofton, M., Hurtt, G., Kellner, J., Luthcke, S., Armston, J., Tang, H., Duncanson, L., Hancock, S., Jantz, P., Marselis, S., Patterson, P.L., Qi, W., Silva, C., 2020. The global ecosystem dynamics investigation: high-resolution laser ranging of the Earth's forests and topography. Sci. Remote Sens. 1, 100002.

Duro, R., Neubauer, G., Bojor, A.-I., 2021. The potential of monitoring traffic conditions up to 15 times a day using sub-meter resolution EO images. In: EGU General Assembly Conference Abstracts pp. EGU21-12831.

Fraser, C.S., Hanley, H.B., 2003. Bias compensation in rational functions for IKONOS satellite imagery. Photogramm. Eng. Remote Sens. 69, 53–57.

Gamon, J.A., Field, C.B., Goulden, M.L., Griffin, K.L., Hartley, A.E., Joel, G., Penuelas, J., Valentini, R., 1995. Relationships between NDVI, canopy structure, and photosynthesis in three californian vegetation types. Ecol. Appl. 5, 28–41.

Garzaniti, N., Tekic, Z., Kukolj, D., Golkar, A., 2021. Review of technology trends in new space missions using a patent analytics approach. Prog. Aerosp. Sci. 125, 100727.

Gastellu-Etchegorry, J.-P., Demarez, V., Pinel, V., Zagolski, F., 1996. Modeling radiative transfer in heterogeneous 3-d vegetation canopies. Remote Sens. Environ. 58, 131–156.

Gastellu-Etchegorry, J.-P., Yin, T., Lauret, N., Cajgfinger, T., Gregoire, T., Grau, E., Feret, J.-B., Lopes, M., Guilleux, J., Dedieu, G., Malenovský, Z., Cook, B., Morton, D., Rubio, J., Durrieu, S., Cazanave, G., Martin, E., Ristorcelli, T., 2015. Discrete anisotropic radiative transfer (DART 5) for modeling airborne and satellite spectroradiometer and LIDAR acquisitions of natural and urban landscapes. Remote Sens. 7, 1667–1701.

Gastellu-Etchegorry, J.-P., Yin, T., Lauret, N., Grau, E., Rubio, J., Cook, B.D., Morton, D. C., Sun, G., 2016. Simulation of satellite, airborne and terrestrial LiDAR with DART (I): waveform simulation with quasi-Monte Carlo ray tracing. Remote Sens. Environ. 184, 418–435.

Gastellu-Etchegorry, J.P., Lauret, N., Yin, T., Landier, L., Kallel, A., Malenovský, Z., Bitar, A.A., Aval, J., Benhmida, S., Qi, J., Medjdoub, G., Guilleux, J., Chavanon, E., Cook, B., Morton, D., Chrysoulakis, N., Mitraka, Z., 2017. DART: recent advances in remote sensing data modeling with atmosphere, polarization, and chlorophyll fluorescence. IEEE J. Sel. Top. Appl. Earth Obs. Remote Sens. 10, 2640–2649.

Goldbergs, G., Maier, S.W., Levick, S.R., Edwards, A., 2019. Limitations of high resolution satellite stereo imagery for estimating canopy height in australian tropical savannas. Int. J. Appl. Earth Obs. Geoinf. 75, 83–95.

Grau, E., Gastellu-Etchegorry, J.-P., 2013. Radiative transfer modeling in the earth-atmosphere system with DART model. Remote Sens. Environ. 139, 149–170.

Hall, F.G., Bergen, K., Blair, J.B., Dubayah, R., Houghton, R., Hurtt, G., Kellndorfer, J., Lefsky, M., Ranson, J., Saatchi, S., Shugart, H.H., Wickland, D., 2011. Characterizing 3D vegetation structure from space: Mission requirements. Remote Sens. Environ. 115, 2753–2775.

Harding, D.J., Carabajal, C.C., 2005. ICESat waveform measurements of within-footprint topographic relief and vegetation vertical structure. Geophys. Res. Lett. 32.

Howat, I.M., Porter, C., Smith, B.E., Noh, M.J., Morin, P., 2019. The reference elevation model of Antarctica. Cryosphere 13, 665–674.

Hugonnet, R., McNabb, R., Berthier, E., Menounos, B., Nuth, C., Girod, L., Farinotti, D., Huss, M., Dussaillant, I., Brun, F., Kääb, A., 2021. Accelerated global glacier mass loss in the early twenty-first century. Nature 592, 726–731.

Jeong, J., Kim, T., 2016. Quantitative estimation and validation of the effects of the convergence, bisector elevation, and asymmetry angles on the positioning accuracies of satellite stereo pairs. Photogramm. Eng. Remote Sens. 82, 625–633.

Jérôme, S., 2019. Shaping the future of earth observation with Pléiades Neo. In: 2019 9th International Conference on Recent Advances in Space Technologies (RAST), pp. 399–401.

Jiang, H., Cheng, S., Yan, G., Kuusk, A., Hu, R., Tong, Y., Mu, X., Xie, D., Zhang, W., Zhou, G., Morsdorf, F., 2021. Clumping effects in leaf area index retrieval from large-footprint full-waveform LiDAR. IEEE Trans. Geosci. Remote Sens. 1–20.

Kolb, K., Choi, H.-S., Kaur, B., Olson, J., Hill, C., Hutchinson, J., 2016. Digital imaging and remote sensing image generator (DIRSIG) as applied to NVESD sensor performance modeling. SPIE.

Langford, E., 2006. Quartiles in elementary statistics. J. Stat. Educ. 14 null-null.

Lazaros, N., Sirakoulis, G.C., Gasteratos, A., 2008. Review of stereo vision algorithms: from software to hardware. Int. J. Optomech. 2, 435–462.

Le Toan, T., Quegan, S., Davidson, M., Balzter, H., Paillou, P., Papathanassiou, K., Plummer, S., Rocca, F., Saatchi, S., Shugart, H., 2011. The BIOMASS mission: mapping global forest biomass to better understand the terrestrial carbon cycle. Remote Sens. Environ. 115, 2850–2860.

Lebègue, L., Cazala-Hourcade, E., Languille, F., Artigues, S., Melet, O., 2020. CO3D, a worldwide one one-meter accuracy dem for 2025. In: The International Archives of Photogrammetry, Remote Sensing and Spatial Information Sciences, 43, pp. 299–304.

Li, D., Wang, M., Jiang, J., 2021. China's high-resolution optical remote sensing satellites and their mapping applications. Geo-spat. Inform. Sci. 24, 85–94.

Liu, A., Cheng, X., Chen, Z., 2021. Performance evaluation of GEDI and ICESat-2 laser altimeter data for terrain and canopy height retrievals. Remote Sens. Environ. 264, 112571.

Malambo, L., Popescu, S.C., 2021. Assessing the agreement of ICESat-2 terrain and canopy height with airborne lidar over US ecozones. Remote Sens. Environ. 266, 112711.

Markus, T., Neumann, T., Martino, A., Abdalati, W., Brunt, K., Csatho, B., Farrell, S., Fricker, H., Gardner, A., Harding, D., Jasinski, M., Kwok, R., Magruder, L., Lubin, D., Luthcke, S., Morison, J., Nelson, R., Neuenschwander, A., Palm, S., Popescu, S., Shum, C.K., Schutz, B.E., Smith, B., Yang, Y., Zwally, J., 2017. The ice, cloud, and land elevation Satellite-2 (ICESat-2): science requirements, concept, and implementation. Remote Sens. Environ. 190, 260–273.

Montesano, P.M., Neigh, C., Sun, G., Duncanson, L., Van Den Hoek, J., Ranson, K.J., 2017. The use of sun elevation angle for stereogrammetric boreal forest height in open canopies. Remote Sens. Environ. 196, 76–88.

Montesano, P.M., Neigh, C.S.R., Wagner, W., Wooten, M., Cook, B.D., 2019. Boreal canopy surfaces from spaceborne stereogrammetry. Remote Sens. Environ. 225, 148–159.

Moratto, Z.M., Broxton, M.J., Beyer, R.A., Lundy, M., Husmann, K., 2010. Ames Stereo Pipeline, NASA's open source automated stereogrammetry software. In: Lunar and Planetary Science Conference, p. 2364.

Morin, P., Porter, C., Cloutier, M., Howat, I., Noh, M.-J., Willis, M., Bates, B., Willamson, C., Peterman, K., 2016. ArcticDEM; A Publically Available, High Resolution Elevation Model of the Arcti pp. EPSC2016-8396.

Morton, D.C., Nagol, J., Carabajal, C.C., Rosette, J., Palace, M., Cook, B.D., Vermote, E.F., Harding, D.J., North, P.R.J., 2014. Amazon forests maintain consistent canopy structure and greenness during the dry season. Nature 506, 221–224.

NASA, 2021. Observing Earth's changing surface topography and vegetation structure – A frame work for the decade, NASA's surface topography and vegetation incubation study white paper.

Neigh, C.S.R., Masek, J.G., Bourget, P., Cook, B., Huang, C., Rishmawi, K., Zhao, F., 2014. Deciphering the precision of stereo IKONOS canopy height models for US forests with G-LiHT airborne LiDAR. Remote Sens. 6, 1762–1782.

Neigh, C.S.R., Masek, J.G., Bourget, P., Rishmawi, K., Zhao, F., Huang, C., Cook, B.D., Nelson, R.F., 2016. Regional rates of young US forest growth estimated from annual landsat disturbance history and IKONOS stereo imagery. Remote Sens. Environ. 173, 282–293.

Neuenschwander, A., Pitts, K., 2019. The ATL08 land and vegetation product for the ICESat-2 Mission. Remote Sens. Environ. 221, 247–259.

Neumann, T.A., Martino, A.J., Markus, T., Bae, S., Bock, M.R., Brenner, A.C., Brunt, K.M., Cavanaugh, J., Fernandes, S.T., Hancock, D.W., Harbeck, K., Lee, J., Kurtz, N.T., Luers, P.J., Luthcke, S.B., Magruder, L., Pennington, T.A., Ramos-Izquierdo, L., Rebold, T., Skoog, J., Thomas, T.C., 2019. The ice, cloud, and land elevation satellite – 2 mission: a global geolocated photon product derived from the advanced topographic laser altimeter system. Remote Sens. Environ. 233, 111325.

Ni, W., Yu, T., Pang, Y., Zhang, Z., He, Y., Li, Z., Sun, G., 2023. Seasonal effects on aboveground biomass estimation in mountainous deciduous forests using ZY-3 stereoscopic imagery. Remote Sens. Environ. 289, 113520.

Ni, W., Zhang, Z., Sun, G., Liu, Q., 2019. Modeling the stereoscopic features of mountainous Forest landscapes for the extraction of Forest Heights from stereo imagery. Remote Sens. 11, 1222.

Paruelo, J.M., Golluscio, R.A., Guerschman, J.P., Cesa, A., Jouve, V.V., Garbulsky, M.F., 2004. Regional scale relationships between ecosystem structure and functioning: the case of the patagonian steppes. Glob. Ecol. Biogeogr. 13, 385–395.

Perko, R., Raggam, H., Gutjahr, K., Schardt, M., 2014. Assessment of the mapping potential of Pléiades stereo and triplet data. In: ISPRS Annals of the Photogrammetry, Remote Sensing and Spatial Information Sciences, 2, p. 103.

Persson, H.J., Perko, R., 2016. Assessment of boreal forest height from WorldView-2 satellite stereo images. Remote Sens. Lett. 7, 1150–1159.

Piermattei, L., Marty, M., Karel, W., Ressl, C., Hollaus, M., Ginzler, C., Pfeifer, N., 2018. Impact of the acquisition geometry of very high-resolution Pléiades imagery on the accuracy of canopy height models over forested alpine regions. Remote Sens. 10, 1542.

Pomerleau, F., Colas, F., Siegwart, R., Magnenat, S., 2013. Comparing ICP variants on real-world data sets. Auton. Robot. 34, 133–148.

Porter, C., Morin, P., Howat, I., Noh, M.-J., Bates, B., Peterman, K., Keesey, S., Schlenk, M., Gardiner, J., Tomko, K., 2018. ArcticDEM. Harvard Dataverse, 1, 2018-2030.2008.

Purves, D., Pacala, S., 2008. Predictive models of Forest dynamics. Science 320, 1452–1453.

Qi, W., Dubayah, R.O., 2016. Combining tandem-X InSAR and simulated GEDI lidar observations for forest structure mapping. Remote Sens. Environ. 187, 253–266.

Qin, R., 2019. A critical analysis of satellite stereo pairs for digital surface model generation and a matching quality prediction model. ISPRS J. Photogramm. Remote Sens. 154, 139–150.

Quegan, S., Le Toan, T., Chave, J., Dall, J., Exbrayat, J.-F., Minh, D.H.T., Lomas, M., D'Alessandro, M.M., Paillou, P., Papathanassiou, K., Rocca, F., Saatchi, S., Scipal, K., Shugart, H., Smallman, T.L., Soja, M.J., Tebaldini, S., Ulander, L., Villard, L., Williams, M., 2019. The European Space Agency BIOMASS mission: measuring forest above-ground biomass from space. Remote Sens. Environ. 227, 44–60.

Roujean, J.-L., Leroy, M., Deschamps, P.-Y., 1992. A bidirectional reflectance model of the Earth's surface for the correction of remote sensing data. J. Geophys. Res. Atmos. 97, 20455–20468.

Schaepman-Strub, G., Schaepman, M.E., Painter, T.H., Dangel, S., Martonchik, J.V., 2006. Reflectance quantities in optical remote sensing—definitions and case studies. Remote Sens. Environ. 103, 27–42.

Schutz, B.E., Zwally, H.J., Shuman, C.A., Hancock, D., DiMarzio, J.P., 2005. Overview of the ICESat Mission. Geophys. Res. Lett. 32.

Shean, D.E., Alexandrov, O., Moratto, Z.M., Smith, B.E., Joughin, I.R., Porter, C., Morin, P., 2016. An automated, open-source pipeline for mass production of digital elevation models (DEMs) from very-high-resolution commercial stereo satellite imagery. ISPRS J. Photogramm. Remote Sens. 116, 101–117.

Shean, D.E., Bhushan, S., Montesano, P., Rounce, D.R., Arendt, A., Osmanoglu, B., 2020. A systematic, regional assessment of high mountain Asia glacier mass balance. Front. Earth Sci. 7.

Shean, D.E., Joughin, I.R., Dutrieux, P., Smith, B.E., Berthier, E., 2019. Ice shelf basal melt rates from a high-resolution digital elevation model (DEM) record for Pine Island glacier, Antarctica. Cryosphere 13, 2633–2656.

Simard, M., Pinto, N., Fisher, J.B., Baccini, A., 2011. Mapping forest canopy height globally with spaceborne lidar. Journal of geophysical research. Biogeosciences 116.

St-Onge, B., Hu, Y., Vega, C., 2008. Mapping the height and above-ground biomass of a mixed forest using lidar and stereo Ikonos images. Int. J. Remote Sens. 29, 1277–1294.

Tong, X., Ye, Z., Xu, Y., Tang, X., Liu, S., Li, L., Xie, H., Wang, F., Li, T., Hong, Z., 2014. Framework of jitter detection and compensation for high resolution satellites. Remote Sens. 6, 3944–3964.

Toutin, T., 2004. Comparison of stereo-extracted DTM from different high-resolution sensors: SPOT-5, EROS-a, IKONOS-II, and QuickBird. IEEE Trans. Geosci. Remote Sens. 42, 2121–2129.

Wang, M., Zhu, Y., Jin, S., Pan, J., Zhu, Q., 2016. Correction of ZY-3 image distortion caused by satellite jitter via virtual steady reimaging using attitude data. ISPRS J. Photogramm. Remote Sens. 119, 108–123.

Wang, Y., Kallel, A., Yang, X., Regaieg, O., Lauret, N., Guilleux, J., Chavanon, E., Gastellu-Etchegorry, J.-P., 2022. DART-lux: an unbiased and rapid Monte Carlo radiative transfer method for simulating remote sensing images. Remote Sens. Environ. 274, 112973.

Wei, S., Yin, T., Dissegna, M.A., Whittle, A.J., Ow, G.L.F., Yusof, M.L.M., Lauret, N., Gastellu-Etchegorry, J.-P., 2020. An assessment study of three indirect methods for estimating leaf area density and leaf area index of individual trees. Agric. For. Meteorol. 292–293, 108101.

Winsemius, H.C., Ward, P.J., Gayton, I., ten Veldhuis, M.-C., Meijer, D.H., Iliffe, M., 2019. Commentary: the need for a high-accuracy, open-access global DEM. Front. Earth Sci. 7.

Wu, S., Wen, J., Gastellu-Etchegorry, J.-P., Liu, Q., You, D., Xiao, Q., Hao, D., Lin, X., Yin, T., 2019. The definition of remotely sensed reflectance quantities suitable for rugged terrain. Remote Sens. Environ. 225, 403–415.

Yan, G., Hu, R., Luo, J., Weiss, M., Jiang, H., Mu, X., Xie, D., Zhang, W., 2019. Review of indirect optical measurements of leaf area index: recent advances, challenges, and perspectives. Agric. For. Meteorol. 265, 390–411.

Yang, X., Wang, Y., Yin, T., Wang, C., Lauret, N., Regaieg, O., Xi, X., Gastellu-Etchegorry, J.P., 2022. Comprehensive LiDAR simulation with efficient physically-based DART-lux model (I): theory, novelty, and consistency validation. Remote Sens. Environ. 272, 112952.

Yin, T., Cook, B.D., Morton, D.C., 2022. Three-dimensional estimation of deciduous forest canopy structure and leaf area using multi-directional, leaf-on and leaf-off airborne lidar data. Agric. For. Meteorol. 314, 108781.

Yin, T., Gastellu-Etchegorry, J.P., Grau, E., Lauret, N., Rubio, J., 2013. Simulating satellite waveform Lidar with DART model. In: 2013 IEEE International Geoscience and Remote Sensing Symposium - IGARSS, pp. 3029–3032.

Yin, T., Lauret, N., Gastellu-Etchegorry, J.-P., 2015. Simulating images of passive sensors with finite field of view by coupling 3-D radiative transfer model and sensor perspective projection. Remote Sens. Environ. 162, 169–185.

Yin, T., Lauret, N., Gastellu-Etchegorry, J.-P., 2016. Simulation of satellite, airborne and terrestrial LiDAR with DART (II): ALS and TLS multi-pulse acquisitions, photon counting, and solar noise. Remote Sens. Environ. 184, 454–468.

Yin, T., Montesano, P.M., Cook, B.D., Chavanon, E., Neigh, C.S.R., Lauret, N., Peng, D., Regaieg, O., Morton, D.C., Gastellu-Etchegorry, J.-P., 2023. Modeling forest canopy surface retrievals using very high-resolution spaceborne stereogrammetry: (I) methods and actual data comparisons. Remote Sens. Environ. (In press).

Yin, T., Qi, J., Cook, B.D., Morton, D.C., Wei, S., Gastellu-Etchegorry, J.-P., 2020. Modeling small-footprint airborne lidar-derived estimates of gap probability and leaf area index. Remote Sens. 12, 4.

Zhao, L., Fang, Z., Chu, Q., 2022. Preliminary Evaluation of the Stereo Mapping Accuracy of the Gaofen-7. In: Wang, L., Wu, Y., Gong, J. (Eds.), Proceedings of the 7th China High Resolution Earth Observation Conference (CHREOC 2020). Springer Nature Singapore, Singapore, pp. 303–320.

Zwally, H.J., Schutz, B., Abdalati, W., Abshire, J., Bentley, C., Brenner, A., Bufton, J., Dezio, J., Hancock, D., Harding, D., Herring, T., Minster, B., Quinn, K., Palm, S., Spinhirne, J., Thomas, R., 2002. ICESat's laser measurements of polar ice, atmosphere, ocean, and land. J. Geodyn. 34, 405–445.